Isotopic Constraints on the Nature of Primary Precipitates in Archean–Early Paleoproterozoic Iron Formations from Determinations of the Iron Phonon Density of States of Greenalite and 2L- and 6L-Ferrihydrite

Andy W Heard, Nicolas Dauphas, Isaac L Hinz, Jena E Johnson, Marc Blanchard, Esen E Alp, Michael Y Hu, Jiyong Zhao, Barbara Lavina, Mark E Fornace, et al.

▶ To cite this version:

Andy W Heard, Nicolas Dauphas, Isaac L Hinz, Jena E Johnson, Marc Blanchard, et al.. Isotopic Constraints on the Nature of Primary Precipitates in Archean–Early Paleoproterozoic Iron Formations from Determinations of the Iron Phonon Density of States of Greenalite and 2L- and 6L-Ferrihydrite. ACS Earth and Space Chemistry, 2023, ⟨10.1021/acsearthspacechem.2c00313⟩. ⟨hal-04044631⟩

HAL Id: hal-04044631
https://hal.science/hal-04044631v1

Submitted on 24 Mar 2023

Isotopic constraints on the nature of primary precipitates in Archean-early Paleoproterozoic iron formations from determinations of the iron phonon density of states of greenalite, and 2L- and 6L-ferrihydrite.

Andy W. Heard[1,2,3,], Nicolas Dauphas[1], Isaac L. Hinz[4], Jena E. Johnson[4], Marc Blanchard[5], Esen E. Alp[6], Michael Y. Hu[6], Jiyong Zhao[6], Barbara Lavina[6,7], Mark E. Fornace[1,8], Justin Y. Hu[1,9], Mathieu Roskosz[10], Corliss Kin I Sio[11], Nicole X. Nie[12], Benoît Baptiste[10].*

**Corresponding author: andrew.heard@whoi.edu*

[1]Origins Laboratory, Department of the Geophysical Sciences and Enrico Fermi Institute, The University of Chicago, Chicago, IL 60637, USA.

[2]Department of Geology & Geophysics, Woods Hole Oceanographic Institution, Woods Hole, MA 02536, USA.

[3]NIRVANA Laboratories, Woods Hole Oceanographic Institution, Woods Hole, MA, 02536 USA.

[4]Department of Earth and Environmental Sciences, University of Michigan, 1100 North University Avenue, Ann Arbor, MI 48109, USA.

[5]Géosciences Environnement Toulouse (GET), Observatoire Midi-Pyrénées,s, CNRS, IRD, CNES, UPS, 14 Avenue Edouard Belin, Toulouse 31400, France.

[6]Advanced Photon Source, Argonne National Laboratory, 9700 South Cass Avenue, Argonne, IL 60439, USA.

[7]Center for Advanced Radiation Sources, The University of Chicago, Chicago, IL 60439, USA

[8]Division of Chemistry & Chemical Engineering, California Institute of Technology, Pasadena, CA 91125, USA.

[9]Department of Earth Sciences, University of Cambridge, Downing Street, Cambridge CB2 3EQ, UK.

[10]Institut de Minéralogie, de Physique des Matériaux et de Cosmochimie, Sorbonne Université, 4 Place Jussieu, Paris 75005, France.

[11]Department of Earth Sciences, University of Toronto, Ontario, Canada

[12]The Isotoparium, Division of Geological and Planetary Sciences, California Institute of Technology, Pasadena, CA 91125, USA.

KEYWORDS

Iron Formations

Iron Isotopes

Greenalite

Ferrihydrite

Great Oxidation Event

Iron phonon density of states

ABSTRACT (249 words)

Iron formations (IFs) are chemical sedimentary rocks that were widely deposited before the Great Oxidation Event (GOE) at 2.4-2.2 Ga. It is generally thought that IFs precipitated as hydrated Fe^{3+} oxides (HFOs) such as ferrihydrite following surface oxidation of Fe^{2+}-rich, anoxic deep waters. This model often implicates biological oxidation and underpins reconstructions of marine nutrient concentrations. However, nanoscale petrography indicates that an Fe^{2+} silicate, greenalite, is a common primary mineral in well-preserved IFs, motivating an alternative depositional model of anoxic ferrous silicate precipitation. It is unclear however if Fe^{2+}-rich silicates can produce the Fe isotopic variations in IFs that are well explained by Fe^{2+} oxidation. To address this question, we constrain the equilibrium Fe isotopic ($^{56}Fe/^{54}Fe$) fractionation of greenalite and ferrihydrite, by determining the iron phonon densities of states for those minerals. We use *ab initio* Density Functional Theory (DFT + U) calculations and Nuclear Resonant Inelastic X-Ray Scattering (NRIXS) spectroscopy, to show that ferrous greenalite should be isotopically lighter than ferrihydrite by ~1-1.2 ‰ at equilibrium, and fractionation should scale linearly with increasing Fe^{3+} content in greenalite. By anchoring ferrihydrite-greenalite mineral pair fractionations to published experimental Fe isotopic fractionations between HFOs and aqueous Fe^{2+}, we show that ferrous greenalite may produce all but the heaviest pre-GOE Fe isotopic compositions and mixed valence greenalites can produce the entire record. Our results suggest that heavy Fe isotope enrichments are not diagnostic of primary IF mineralogies, and ferrihydrite, partially oxidized or even purely ferrous greenalite are all viable primary mineralogies IFs.

MAIN TEXT (9312 words)

1. INTRODUCTION

Until ~2.43 billion years ago (Ga), Earth's atmosphere was practically devoid of free oxygen (O_2)[1–3]. Prior to the Great Oxidation Event (GOE) beginning around 2.43 Ga, and for substantial periods of time after it, the oceans were largely anoxic[4], and had high concentrations of dissolved Fe^{2+} and silica ($SiO_{2(aq)}$). The large marine Fe^{2+} pool was likely sourced predominantly from seafloor hydrothermal vents[5–9], with contributions from anoxic continental weathering[6,10,11]. Widespread iron formations (IFs), distinctive chemical sedimentary rocks rich in Fe and Si, are a hallmark of pre-GOE sedimentary rocks (Fig. 1)[6,12–14]. Most IFs preceding the GOE are banded iron formations (BIFs), characterized by compositional layering at scales ranging from sub-mm rhythmic microbands of alternating Fe-rich and silica-rich minerals, to meter-scale macrobands defining facies transitions during major accumulations over millions of years (Fig. 1)[15]. The mineralogy of IFs is diverse, and can be broadly categorized into oxides dominated by magnetite [Fe_3O_4] and hematite [Fe_2O_3], Fe-rich carbonates, and the Fe silicates greenalite [$(Fe^{2+}, Fe^{3+})_{2\text{-}3}Si_2O_5(OH)_4$], minnesotaite [$Fe_3Si_4O_{10}(OH)_2$] and stilpnomelane [$K(Fe^{2+}, Mg, Fe^{3+})_8(Si, Al)_{12}(O, OH)_{27}\cdot n(H_2O)$], all accompanied by ubiquitous chert (SiO_2). The precursors to these minerals were precipitated from ancient oceans, but it is widely recognized that the present-day mineralogy of IFs is almost entirely secondary in nature—a result of prolonged early and late diagenesis, metamorphism, and interactions with fluids over their several-billion year histories[13,14,16]. The canonical interpretation is that the primary precipitates were amorphous silica and hydrous ferric oxides (HFOs), with the latter formed through the oxidation of Fe^{2+} and rapid precipitation of insoluble Fe^{3+} as oxyhydroxide phases[17]. Possible oxidants for Fe^{2+} include O_2 (produced by early-evolved cyanobacteria)[17], UV photons[18–20], and direct Fe^{2+} oxidation by anoxygenic photosynthesis[21–23], all of which would most likely have operated in the photic zone and thus restrict Fe precipitation to shallower waters supplied with Fe^{2+} upwelled from depth.

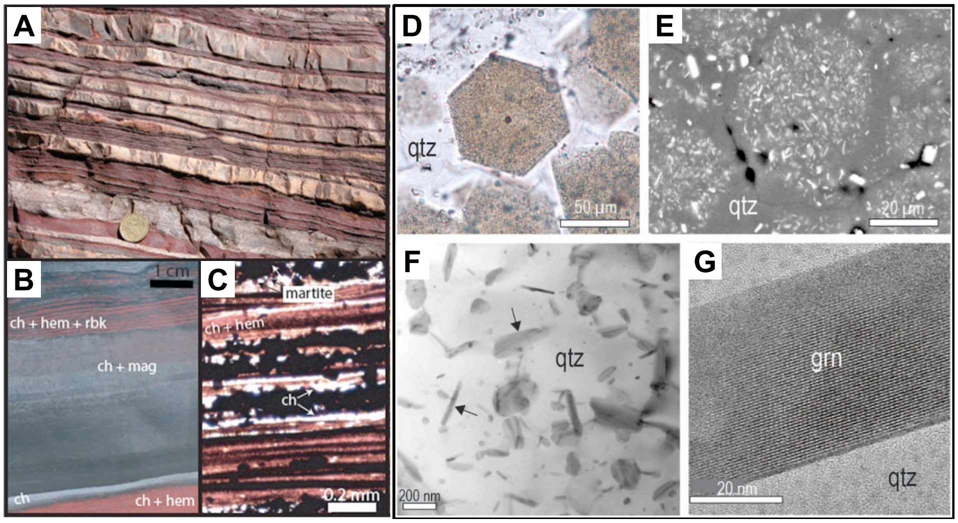

Figure 1. Images of pre-GOE iron formations (IFs) at various scales. **A.** Centimeter scale banding in the Joffre Member of the 2.46 Ga Brockman IF, in the Hamersley basin, Australia **B.** Micro- and mesobanding, with chert, hematite, and riebeckite, microbanded layers and thicker chert and magnetite layers in the Joffre Member. **C.** Photomicrograph showing thin chert-hematite microbands, and coarser magnetite microbands (thick black layers) in the Joffre Member. **D.** Photomicrograph of greenalite-rich hexagonal chert pod surrounded by Fe-poor chert, from the 2.48 Ga Klein Naute Formation, Griqualand West Basin South Africa. **E.** Backscattered electron image from the 2.56 Ga Bee Gorge Member, Witenoom Formation, Hamersley basin, Australia. **F.** Bright-field transmission electron microscope (TEM) image from the Bee Gorge Member. **G.** High-resolution TEM image of greenalite nano particles, from the 2.56 Ga Bee Gorge Member. Images **A-C** from Konhauser et al. Iron Formations: A Global Record of Neoarchaean to Palaeoproterozoic Environmental History. *Earth-Science Reviews.* **2017**, *172*, 140–177. Copyright (2017) Elsevier. Images **D-G** from Rasmussen et al. Greenalite and Its Role in the Genesis of Early Precambrian Iron Formations – A Review. *Earth-Science. Reviews.* **2021**, 103613. Copyright (2021) Elsevier.

While IFs contain appreciable Fe^{3+}, they have an average Fe valence state of ~2.4+ (60% Fe^{2+} and 40% Fe^{3+})[16]. This is evident both at the bulk scale, where IFs contain a variety of ferric and ferrous minerals, and in mixed-valence Fe minerals like magnetite [$Fe^{3+}{}_2Fe^{2+}O_4$]. In the HFO model, much of the Fe^{2+} content in IFs is attributed to early or late diagenetic reduction of Fe^{3+} during the oxidation of organic matter, such as through microbial dissimilatory Fe^{3+} reduction (DIR) or metasomatic reactions during burial heating[24–28]. The Fe^{2+} produced by these reactions may have reacted with the remaining HFOs to form magnetite, or precipitated directly as Fe carbonate (siderite) or Fe^{2+} silicates as early diagenetic phases[14,29–31]. Organic carbon is present in very low abundance in IFs[32], possibly because it was respired away by reduction of excess Fe^{3+}.

Assumptions related to the Fe^{2+} oxidation model for IFs underpin most interpretations of the chemistry of the oceans prior to the GOE. The model prescribes an oceanic redox structure characterized by reducing deep marine basins enriched in Fe^{2+} sourced from hydrothermal vents, and near-surface waters that were sufficiently oxidizing to precipitate HFOs. This primary precipitation of HFOs is also a key assumption of approaches used to quantitatively estimate concentrations of key nutrient elements in the Precambrian oceans from the geochemical archive of IFs[33–38]. These studies used experimentally calibrated nutrient element partitioning on HFOs to estimate seawater concentrations from geochemical analyses of IFs, most notably for phosphorous (P)[33,34,37], the main limiting macronutrient over geological timescales, and nickel (Ni)[35,36], a critical co-factor for methanogenesis.

Recently, the HFO model for IFs has been challenged by an alternative hypothesis in which the precursor mineralogy for Archean IFs and Fe-oxide-rich cherts was entirely composed of nominally Fe^{2+}-dominated hydrous silicates, such greenalite $Fe^{2+}{}_3Si_2O_5(OH)_4$, with other Fe^{3+} phases such as oxides and mixed-valence silicates reflecting late oxidative metamorphic overprints[39–43]. This new model for IF precursors is founded on a growing number of nanoscale observations of chert bands and nodules in IFs from 3.5-2.4 Ga and predominantly in the Hamersley Basin of Western Australia and the Transvaal Basin of South Africa that suggest Fe silicates, not Fe-oxides, are the earliest-formed surviving minerals in IFs[43–47]. Nanoscale imaging techniques and elemental mapping in those studies specifically targeted chert bands and nodules where early diagenetic silicification preserved delicate microstructures shortly after deposition (Fig. 1D-G). These inclusions were identified as abundant nanoscale (10 nm × 200-1000 nm) particles of greenalite[47,48]. The endmember interpretation of this primary greenalite mineralogy requires that the oceans were fully anoxic during IF deposition, with Fe^{2+} greenalite being the dominant mode of primary Fe precipitation in an ocean without the formation of insoluble Fe^{3+} phases[40,45].

While greenalite has the nominal chemical formula $Fe^{2+}{}_3Si_2O_5(OH)_4$ it can contain appreciable structural Fe^{3+}, as a result of natural syn- and post-depositional processes[39]. A more nuanced picture comes from analysis of the redox state of Fe in greenalite in IFs. Using synchrotron-based Fe L-edge X-ray absorption spectroscopy (XAS) to determine the Fe^{3+}/Fe_{tot} (Fe_{tot} = total Fe) ratio in individual greenalite grains in well-preserved 2.5 Ga IFs, greenalite nanoparticles were found to have Fe^{3+} content of 10-20 % of their total Fe[39]. If the Fe^{3+} in these minerals reflects primary incorporation of Fe^{3+} formed in the ancient water column, this would relax the endmember 'zero oxidation' greenalite interpretation that the pre-GOE oceans were devoid of Fe^{2+} oxidants, and allow for the partial oxidation of Fe^{2+} during IF deposition[39]. Regardless of whether the silicates were entirely ferrous or a ferrous-ferric mix, if the precursor material for IFs prior to the GOE was dominated by silicates, then reconstructions of marine nutrient concentrations based on HFO adsorption experiments may be incorrect, and revision of these estimates would require similar adsorption experiments to be conducted with relevant authigenic silicates.

Given the major implications of primary IF precipitates for our understanding of early marine chemistry, a diagnostic tool that can distinguish between different precursor phases for IFs would be valuable for confirming or ruling out endmember models. Iron isotope geochemistry potentially has this elucidative capability. Iron isotopes are strongly fractionated at low temperature by redox processes and they are resistant to resetting by metamorphism, thus preserving primary sedimentary signals in ancient rocks with complex histories (specifically demonstrated for IFs by Frost et al.[49]). Furthermore, an extensive archive of Fe isotopic measurements of IFs and Fe-oxide-rich cherts spanning > 3 Ga of Earth history is readily available to test different IF precursor hypotheses (Fig. 2)[50,51]. IFs show large variations in the isotopic composition of Fe at bulk rock and mineral scales. The most striking Fe isotopic feature of IFs pre-dating the Great Oxidation Event (GOE) is the prevalence of highly positive δ^{56}Fe values. These positive values have long been taken as evidence for partial Fe^{2+} oxidation in the Archean oceans, because oxidation induces a strong fractionation in Fe isotopes that partitions isotopically heavy Fe into Fe^{3+} relative to Fe^{2+}. Even the most ancient IF occurrences from Isua (SW Greenland) and Nuvvuagittuq (Québec, Canada) (~3.7-3.8 Ga) are characterized by clear heavy Fe isotopic enrichments[52–54], while younger IFs spanning the Archean and early Paleoproterozoic up to the GOE exhibit a wide range of heavy and light Fe isotopic enrichments[51].

The partial oxidation interpretation of the IF Fe isotope record is supported by numerous examples in experiments, and nature, of heavy Fe isotopic enrichment during the oxidation of Fe^{2+} to HFOs. The δ^{56}Fe of the solid HFO phase can be shifted heavier by 1-3 ‰ relative to the Fe^{2+} in solution[20,55–59]. Meanwhile, experimental precipitation of Fe^{2+}/ Fe^{3+} green rusts and the Fe carbonate siderite found a small Fe isotopic fractionation between dissolved and precipitated Fe^{2+}

that enriched most solids in the lighter Fe isotopes[60]. The green rust and siderite experiments thus revealed that these phases cannot account for isotopically heavy Fe in IFs. The most parsimonious interpretation for the heavy Fe isotope enrichments measured in Archean IFs and Fe-oxide-rich cherts (up to +2.6 ‰)[51,61] is therefore that they formed by partial Fe oxidation[50,51]. The entire Fe isotopic record of IFs can then be explained through partial oxidation, and progressive distillation of an Fe^{2+} reservoir during upwelling.

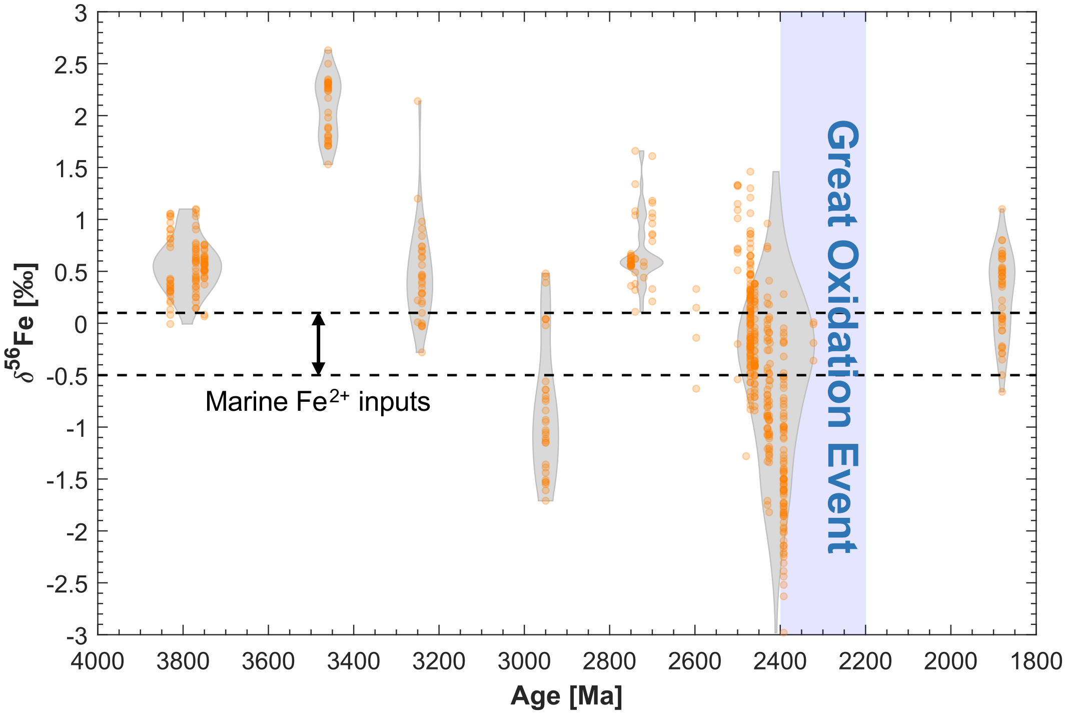

Figure 2. The Fe isotopic record of Archean and Paleoproterozoic iron formations (IFs) and Fe-oxide-rich cherts (modified from Heard and Dauphas, 2020). δ^{56}Fe is the per mil ‰ deviation in the $^{56}Fe/^{54}Fe$ ratio of samples relative to a standard material, IRMM-014 that is isotopically similar to the bulk Earth. Orange circles show individual datapoints. Grey shaded fields (violin plots) show the kernel density of δ^{56}Fe values in 200-million-year time bins centered on the major IFs throughout the Archean and Paleoproterozoic, where the relative width of violin plots is not to scale.

The extent of equilibrium isotopic fractionations between precipitated minerals put forward as IF precursors and dissolved Fe^{2+} remain uncertain. While prior experiments have informed a general expectation for the Fe isotopic behaviors of authigenic ferrous phases, the lack of data for Fe^{2+}-bearing minerals such as greenalite stems in part from the difficulty of running equilibration experiments for minerals that are readily oxidized under modern atmospheric conditions. Another limitation of bulk precipitation experiments is that they can be affected by both equilibrium and kinetic processes. It is therefore important and timely to constrain the equilibrium Fe isotopic fractionation behavior of greenalite relative to ferrihydrite, and dissolved Fe^{2+}. To do this, we employed a combined experimental and computational approach that has proven to be powerful in determining the equilibrium Fe isotopic behavior of other Fe-bearing minerals with relevance to low temperature geochemistry[62,63].

2. MATERIALS AND METHODS

2.1 General approach

Our principal objective is to determine the reduced partition function ratios (also called β factors) for the materials of interest. The β factors for two phases *a* and *b* can be used to determine the equilibrium isotopic fractionation factor $1000 \ln \alpha_{a\text{-}b}$ (in ‰) between them,

$$1000 \ln \alpha_{a\text{-}b} = 1000 \ln \beta_a - 1000 \ln \beta_b. \quad (1)$$

We use a two-pronged approach that combines *ab initio* computations of mineral structures, and nuclear resonant inelastic X-ray scattering (NRIXS), a synchrotron spectroscopic technique, to determine β factors. The use of two independent techniques provides a consistency check and this approach has been applied effectively in earlier works[62,64].

It is nontrivial to calculate the equilibrium fractionation between solid and dissolved species. Iron isotopic fractionations between aqueous and minerals directly calculated using Fe β factors from a combination of *ab initio* simulations (fluids, minerals) and NRIXS measurements (minerals) have the potential to introduce biases associated with their respective computational methods (Dauphas et al.[50] and references therein). Early computational methods used to calculate theoretical Fe β factors for aqueous species[65] have indicated equilibrium fractionations between Fe(II) and Fe(III) that are up to ~2 times those directly observed in Fe isotope equilibration experiments[66,67]; although more recent computations do find better agreement with empirical experiments[68–72]. However, when *ab initio* data for aqueous species are combined with *ab initio* data for mineral species or NRIXS data for mineral species, the calculated β factors fail to reproduce the measured fractionation from fluid-mineral equilibration experiments[63,68–73]. This disagreement appears to derive predominantly from study-to-study variations in the absolute β factor for $Fe(III)_{aq}$[50].

The approach recommended by Dauphas et al.[50] to mitigate these potential biases is to calculate the fractionation factors between different minerals and $Fe(II)_{aq}$ by using mineral-pair equilibrium isotopic fractionations, which are derived from NRXIS or *ab initio* approaches, wherein one mineral in the pair is a reference mineral for which fluid-mineral isotopic equilibration has been directly measured. Here, we take ferrihydrite as the reference mineral in order to calculate the equilibrium $Fe(II)_{aq}$-greenalite fractionation factor that is of interest to understanding the origin of Archean IFs. The fractionation during ferrihydrite (or similar HFO) equilibration with, or precipitation from, Fe(II) solutions has been constrained in numerous studies[20,55–59,66,67,74,75], thus making it a suitable reference phase in calculating the equilibrium Fe isotopic fractionation associated with greenalite precipitation.

Establishing an understanding of the equilibrium isotopic behavior of a mineral phase is the first step in interpreting isotopic fractionation in natural systems because only a few data are needed (nature of the minerals/aqueous species and temperature) to predict equilibrium fractionations between phases. Deviations from the null equilibrium hypothesis can then be attributed to kinetic and/or reservoir effects, which require additional data (mineral zoning, thermal history) to constrain.

2.2. Sample materials for NRIXS

2.2.1. Natural greenalite

A sample of a natural greenalite standard from the San Valentin Ore Body, Murcia, Spain[76] was used for NRIXS analysis. This is, to our knowledge, the naturally occurring greenalite sample with the lowest level of contaminant minerals. After crushing of the rock standard, a greenalite separate was obtained by hand-picking and its identification was confirmed with X-ray diffraction (XRD)[39]. Aliquots of this material have previously been employed as a greenalite standard for XAS investigation of Fe redox states in IF-hosted greenalite[39]. All sample preparation took place on benchtop as the standard was known to be stable in air.

2.2.2. Ferrihydrite

Ferrihydrite samples doped in ^{57}Fe were synthesized in a modified protocol following Schwertmann and Cornell[77], with some departures necessary due to the use of ^{57}Fe metal rather than $Fe(NO_3)_3$ as starting material. Both 2-line (1-3 nm crystallite size) and 6-line (5-6 nm crystallite size) ferrihydrite were synthesized. All aqueous solutions were prepared with MilliQ water (MQ; 18 MΩ). For 2-line ferrihydrite, 85.6 mg of ^{57}Fe (95%, Cambridge Isotope

Laboratories) was dissolved in 3 mL 15.4 M HNO_3 at 100° C for 3 days. The solution was allowed to cool to 25° C, then rapidly titrated with ~30 mL of a 1.5 M NaOH solution to pH 7.0, all while vigorously stirring. The precipitate was collected by centrifuging 10 times at 10-fold dilutions in MQ (10^{10} theoretical dilution overall), followed by drying under a fume hood at 25° C. For 6-line ferrihydrite, 56.5 mg of ^{57}Fe was dissolved in 1.5 mL 11 M $HClO_4$ at 100°C for 2 days. The solution was partially evaporated at 110° C and refilled with 11 M $HClO_4$. This process was repeated 5 times. The solution was evaporated completely at 110°C. The resultant salt was dissolved in 40 mL MQ at 75° C for 10 minutes, then cooled to 25° C in an ice bath. The solution was continuously dialyzed with MQ for 10 days, then freeze dried to isolate the solid.

Characterization of the powders to ensure that 2-line and 6-line ferrihydrite were produced by the syntheses described above was done by XRD and TEM analysis (Fig. 4). X-ray powder diffraction measurements were carried out at the XRD platform of the IMPMC (Paris, France) in transmission geometry, on a Rigaku MM007HF diffractometer equipped with a Mo rotating anode source ($\lambda K\alpha 1 = 0.709319$ Å, $\lambda K\alpha 2 = 0.713609$ Å), Varimax focusing optics and a RAXIS4++ image plate detector. LaB6 standard sample was measured in the same experimental conditions to calibrate the FIT2D program[78], the image processing software used to integrate the intensities around the Debye−Scherrer rings. We performed additional characterization by HR-TEM and selected area electron diffraction (SAED) (Figs. 4C-D). Images were obtained using a FEI Tecnai F30 at 300 kV with a point-to-point resolution of 0.2 nm. TEM samples were prepared using the methods of Janney et al.[79] and placed on porous carbon grids.

2.3. NRIXS analysis of greenalite and ferrihydrite

NRIXS analyses were conducted at Sector 3-ID of the Advanced Photon Source (APS) synchrotron beamline at Argonne National Laboratory in Lemont, IL, USA. NRIXS is a relatively new spectroscopic technique [80,81] that can be used to probe the vibrational properties of select Mössbauer elements in solids. In the case of Fe, NRIXS is effective because ^{57}Fe is a Mössbauer isotope that has a low-lying nuclear excited state at 14.4125 keV. The lifetime of the excited nuclear state is 141 ns for ^{57}Fe, which is long relative to both the duration of electronic scattering of most X-rays (< 1 ps), and the duration of pulsed X-ray flashes provided by the synchrotron source (70 ps pulses, separated by 153 ns). As such, nuclear resonance enables time discrimination to isolate the energy scattering spectrum caused by nuclear transitions.

The vibrational properties of Fe in solids can be probed with the nuclear scattering spectrum. Recoilless elastic scattering produces part of the signal. The remaining inelastic portion of the scattering signal is influenced by the material lattice holding Fe atoms in place. The inelastic scattering spectrum spans a far broader energy range (on the order of +/- 100 meV) than the linewidth of the nuclear transition. When an incident photon has a higher energy than the low-lying excited state of the ^{57}Fe nucleus, excess energy can be dispersed to the solid material lattice by excitation of quantized modes of vibration called phonons (phonon creation). Conversely, X-rays with an energy slightly below that required for the nuclear transition can excite nuclei as well, with vibration in the mineral lattice providing the extra energy (phonon annihilation). After removing the central elastic peak associated with absorption by X-rays at the resonant energy, NRIXS enables probing of the full vibrational spectrum of ^{57}Fe in solids as a function of energy, called the partial phonon density of states (pDOS), or $g(E)$, being ‘partial’ because only the vibrational properties of Fe in the lattice are determined[81]. We can determine β factors either by taking the moments of *g*(E), or the energy scattering spectrum *S*(E)[63,82]. In the case of *S*(E), the formula to determine β factors is,

$$1000\ln\beta \approx 1000\left(\frac{M}{M^{*}}-1\right)\frac{1}{E_{R}}\left[\frac{R_{3}^{S}}{8k^{2}T^{2}}-\frac{R_{5}^{S}-10R_{2}^{S}R_{3}^{S}}{480k^{4}T^{4}}+\frac{R_{7}^{S}+210\left(R_{2}^{S}\right)^{2}R_{3}^{S}-35R_{3}^{S}R_{4}^{S}-21R_{2}^{S}R_{5}^{S}}{20160k^{6}T^{6}}\right], \qquad (2)$$

where M and M^* are the masses of two isotopes of interest (*e.g.* 56 and 54), E_R is the free recoil energy (1.956 meV for ^{57}Fe), T is the temperature, k is the Boltzmann constant, and R_i^S is the ith centered moment of the scattering spectrum *S*(E) where $R_i^S=\int_{-\infty}^{+\infty} S(E)(E-E_R)^i dE$. The equation relating 1000lnβ to *S*(E) was derived by Dauphas et al.[63] and Hu et al.[82]. One can use a mathematically equivalent expression for *g*(E) to determine 1000lnβ[63,82,83],

$$1000\ln\beta \approx 1000\left(\frac{M}{M^{*}}-1\right)\frac{1}{E_{R}}\left[\frac{m_{2}^{g}}{8k^{2}T^{2}}-\frac{m_{4}^{g}}{480k^{4}T^{4}}+\frac{m_{6}^{g}}{20160k^{6}T^{6}}\right], \qquad (3)$$

Where m_j^g is the jth moment of the pDOS *g*(E) where $m_j^g=\int_{0}^{+\infty} E^j g(E)dE$. As discussed by Dauphas et al.[63], the two formulas are mathematically equivalent but *g* is calculated by taking a Fourier-Log transform of *S*[81]. Error assessment is therefore more complicated[62]. Equations 2 and 3 for 1000lnβ fit the general expected functional form for β factors of,

$$1000\ln\beta \approx \frac{A_1}{T^2}+\frac{A_2}{T^4}+\frac{A_3}{T^6}, \qquad (4)$$

where A_1, A_2, and A_3 can be calculated from Equation 2, above.

Alternatively, 1000lnβ can be expressed as a more compact function of the force constant $\langle F\rangle$:

$$1000\ln\beta \approx \frac{B_1\langle F\rangle}{T^2}+\frac{B_2\langle F\rangle^2}{T^4}, \qquad (5)$$

where B_1 is 2904, B_2 is a constant that depends on the pDOS *g*, and the mean force constant $\langle F\rangle$ of bonds that hold Fe in position is given by

$$\langle F\rangle=\frac{M}{E_R\hbar^2}R_3^S, \qquad (6)$$

where $\hbar$ is the reduced Planck's constant. The equation for 1000lnβ can be reduced to just the first term at high temperature. Additionally, Dauphas et al.[63] showed that using a fixed value of 52000 for B_2 introduces less than 0.2 ‰ error at 22 °C, which is smaller than the overall uncertainty of the NRIXS method. While we use the full polynomial expansion (Eqs. 2, 4) to calculate the temperature-dependence of the β-factors, we will initially describe our results in terms of the force constant $\langle F \rangle$ as it is more straightforward to compare a single parameter and this still captures most of the systematics of interest.

NRIXS data were collected by scanning in 0.25 meV steps around the nominal resonance energy using a set of high-resolution monochromators. Scattered X-rays were measured with avalanche photo-diodes (APDs). Natural greenalite and synthesized ferrihydrite were analyzed in different sessions. The natural greenalite sample was scanned over -164 to +164 meV relative to the elastic peak. The 2-line and 6-line ferrihydrite sample powders were scanned over the range -160 to +160 meV relative to the elastic peak. Broad energy scans are used to monitor count rates in the tails of the distribution used for background corrections[84]. Because the synthesis protocol enabled ferrihydrite samples to be prepared with ^{57}Fe-enriched material, they provided stronger signals, and 5 and 7 scans were made for 2-line and 6-line ferrihydrite, respectively. The greenalite contained Fe with natural isotopic abundances, so the concentration of ^{57}Fe was much smaller, and more scans were needed. For the natural greenalite, 14 scans were made. Additionally, Fe^{3+}/Fe_{total} in the natural greenalite standard was determined prior to NRIXS analysis using nuclear forward scattering [85,86], wherein the synchrotron signal was used in place of a traditional Mössbauer source to determine the Mössbauer spectrum of the material in the time domain (Synchrotron Mössbauer Spectroscopy - SMS[87]; Fig. 5).

All NRIXS data were reduced in Mathematica using the SciPhon[84] program designed for this purpose. The SciPhon software outputs many other parameters from the phonon excitation probability density function *S*(E) and the PDOS *g*(E), such as the Lamb-Mössbauer factor, Helmholtz free energy, and vibrational entropy. The values of these parameters are made available in Supplementary Table S1 for future use.

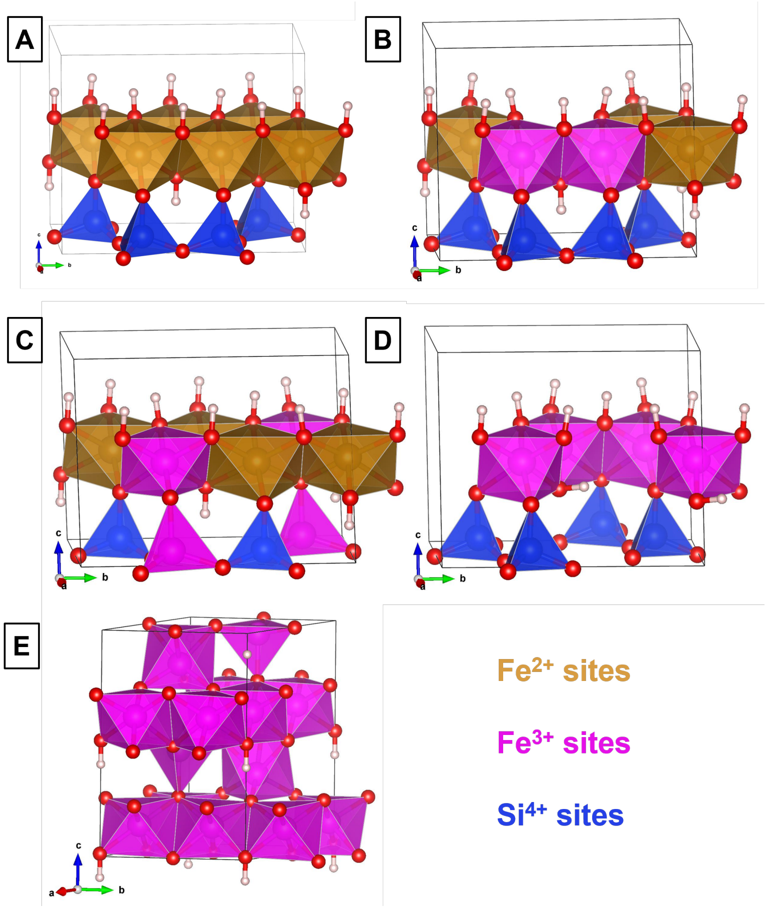

Fig. 3: Crystal structures optimized by DFT+*U*, for **A:** Fe^{2+} greenalite (Gruner, 1936). **B:** $Fe^{2.4+}$ greenalite, constructed assuming a vacancy substitution in 1/6 of octahedral sites ($6Fe^{2+} \leftrightarrow 3Fe^{2+}2Fe^{3+}\square$). **C:** $Fe^{2.5+}$ greenalite, constructed assuming a ferri-Tschermak's substitution ($Fe^{2+}Si^{4+} \leftrightarrow 2Fe^{3+}$). **D:** Fe^{3+} greenalite, constructed assuming a vacancy substitution in 1/3 of octahedral sites ($3Fe^{2+} \leftrightarrow 2Fe^{3+}\square$). **E:** Ferrihydrite from the structural model of Michel et al. (2007).

2.4. Ab initio calculation of reduced partition function ratios for iron in greenalite and ferrihydrite

We conducted *ab initio* density functional theory (DFT) calculations to determine the force constant and reduced partition function ratios for ferrihydrite, and greenalite and related minerals with a range of Fe valence states. For greenalite, we modeled the Fe^{2+} endmember with the monoclinic cell corresponding to the composition $Fe_3Si_2O_5(OH)_4$ (Fig. 3A). Following the observation that Fe^{3+} is predominantly accommodated in octahedral sites in greenalite by vacancy substitution[88], we modeled a mixed valence greenalite ($Fe^{3+}/Fe_{tot} = 0.4$) with a monoclinic cell with one third of octahedral sites occupied by Fe^{3+} (in adjacent sites), compensated by every sixth site being occupied by a vacancy (adjacent to the Fe^{3+} sites) ($Fe^{2+}{}_3Fe^{3+}{}_2\square Si_4O_{10}(OH)_8$) (Fig. 3B). We also explored a mixed-valence ($Fe^{3+}/Fe_{tot} = 0.5$) cronstedtite-like model wherein octahedral Fe^{3+} was compensated by Fe^{3+} substituting for Si^{4+} in tetrahedra (Fig. 3C). This ferri-Tschermak's [$Fe^{2+}Si^{4+} \leftrightarrow 2\ Fe^{3+}$] substitution is observed to be the dominant form of Fe^{3+} incorporation into naturally occurring Mg-rich serpentines[89]. This model is less relevant to the origin of IFs but provides an interesting test of how different modes of Fe^{3+} incorporation impact the Fe force constant and equilibrium isotopic behavior of Fe in serpentines. We modeled an Fe^{3+} endmember for greenalite with a monoclinic structure corresponding to the composition $Fe_2Si_2O_5(OH)_4$ (Fig. 3D). This Fe^{3+} endmember formula for greenalite does not occur naturally, however a very similar mineral, hisingerite ($Fe_2Si_2O_5(OH)_4 \cdot nH_2O$) does occur in nature, associated with low-temperature alteration of ferroan olivine[90]. In hisingerite, charge balance is also maintained by the substitution of octahedral site vacancies, with the end point of this compositional vector being $\square Fe^{3+}{}_2Si_2O_5(OH)_4 \cdot nH_2O$ [90]. We modeled the Fe^{3+} endmember by applying the vacancy substitution to every third Fe site (Fig. 3D). The principal difference between this modeled structure and hisingerite is that hisingerite is hydrated, however the structures are similar, and we might expect that the force constant determined here may be similar to that for hisingerite.

The ferrihydrite (Fe_5O_8H) model was built from the akdalaite hexagonal structure proposed by Michel et al.[91] where Fe atoms are both tetrahedrally and octahedrally coordinated (Fig. 3E). We did not attempt to model the multi-component ferrihydrite model of Drits et al.[92] due to its greater complexity. Most DFT calculations have used the Michel et al.[91] model for the same reason. Sassi et al.[93] recently investigated the two structural models by DFT and concluded that ferrihydrite may be a nanocomposite of the two endmember models proposed by Michel et al.[91] and Drits et al.[92], with the proportions of each structure depending on particle size, temperature, pH, and water partial pressure. Sassi et al.[93] also showed that the Michel and Drits models are thermodynamically equivalent across a wide range of conditions.

Structural relaxations used the PWscf code[94] (http://www.quantum-espresso.org) using the DFT plus Hubbard U method (DFT + U) and the generalized gradient approximation (GGA) to the exchange-correlation functional with the PBE parameterization[95]. The ionic cores were described by ultrasoft pseudopotentials from the Garrity-Bennett-Rabe-Vanderbilt (GBRV) library[96]. After energy convergence tests, the wave-functions and the charge density were expanded in plane-waves with 40 and 400 Ry cutoffs, respectively. For the electronic integration, the Brillouin zone was sampled according to the Monkhorst-Pack scheme[97], using shifted $2 \times 2 \times 2$ k-point grids. Calculations were spin-polarized and magnetic moments were free to relax. The ferrihydrite magnetic ordering was set to be ferrimagnetic, with the Fe-site spins ordering with alternating alignment in layers stacked along the c-direction in the crystallographic unit cell, following the theoretical investigation of Pinney et al.[98]. Greenalite displays antiferromagnetically ordered layers[99]. However, since we used a one-layer unit cell, our model imposed a ferromagnetic structure by periodic repetition of layers with parallel magnetic alignments. The value of the Hubbard *U* for Fe sites was determined using a linear response approach in an internally consistent manner[100,101]. Details of the practical procedure can be found in Blanchard et al.[73].

Following the method reviewed in detail by Blanchard et al.[102], Fe β-factors were calculated from their harmonic vibrational frequencies using

$$\beta(\alpha,\mathrm{Y})=\left[\prod_{\mathrm{i}=1}^{3\mathrm{N_{at}}}\prod_{\{q\}}\frac{\nu^{*}_{q,i}}{\nu_{q,i}}\frac{\mathrm{e}^{-h\nu^{*}_{q,i}/(2k\mathrm{T})}}{1-\mathrm{e}^{-h\nu^{*}_{q,i}/(k\mathrm{T})}}\frac{1-\mathrm{e}^{-h\nu_{q,i}/(k\mathrm{T})}}{\mathrm{e}^{-h\nu_{q,i}/(2k\mathrm{T})}}\right]^{1/(\mathrm{N}_q\mathrm{N})}, \qquad \text{(Eq. 6)}$$

where $\nu_{q,i}$ are the frequencies of the phonon with wavevector q and branch index i = 1, $3\mathrm{N_{at}}$, and where $\mathrm{N_{at}}$ is the number of atoms in the unit cell. $\nu_{q,i}$ and $\nu^{*}_{q,i}$ are the vibrational frequencies in two isotopologues. N is the number of sites for the Y atom in the unit cell, T is the temperature, *h* is the Planck constant and *k* is the Boltzmann constant.

Table 1: Cell parameters optimized by DFT + *U* for modeled greenalite and ferrihydrite compared to experimental data.

	Gr exp*	**Fe^{2+} Gr**	**$Fe^{2.4+}$ Gr (octahedral vacancy substitution)**	**$Fe^{2.5+}$ Gr (Ferri-Tschermak substitution)**	**Fe^{3+} Gr**	**Fh exp***	**Fh**
a (Å)	5.54	5.50	5.45	5.67	5.34	5.95	6.05
b (Å)	9.55	9.53	9.37	9.82	9.28	5.95	6.05
c (Å)	7.44	7.74	7.73	7.43	7.60	9.06	9.40
α (°)	90.0	89.7	90.0	90.7	90.4	90.0	90.0
β (°)	104.2	103.5	103.4	105.4	104.3	90.0	90.0
γ (°)	90.0	90.1	90.0	90.0	89.8	120.0	120.0

*Experimental data for greenalite and ferrihydrite were taken from Gruner (1936) and Michel et al. (2007) respectively.

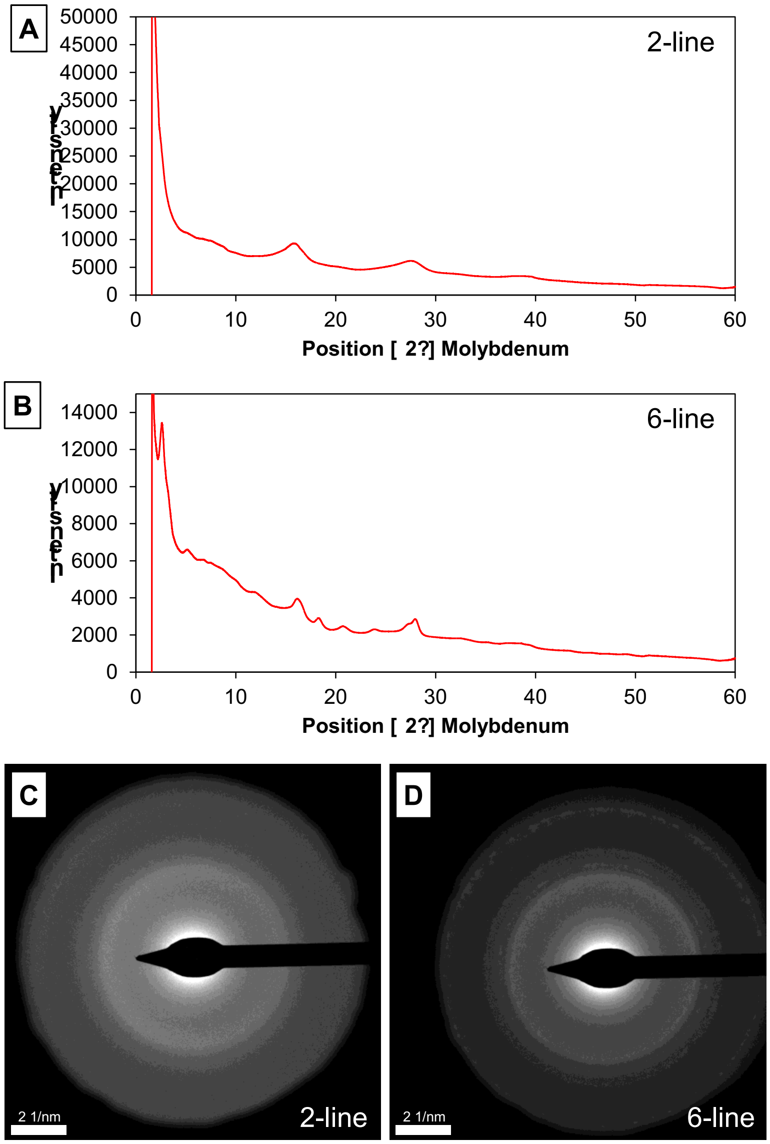

Fig. 4: Structural analysis of synthesized ferrihydrite. **A:** XRD analysis of 2-line ferrihydrite. **B:** XRD analysis of 6-line ferrihydrite. **C:** HR-TEM SAED analysis of 2-line ferrihydrite. **D:** HR-TEM SAED analysis of 6-line ferrihydrite. All patterns agree with published values (Janney et al., 2000; Lee and Xu, 2019).

Phonon frequencies were calculated within the harmonic approximation using the linear response theory[103] as implemented in the PHonon code[94] (http://www.quantum-espresso.org). Phonon frequencies were computed on a centered 2 × 2 × 2 *q*-point grid for ferrihydrite and using one *q*-point shifted with respect to the center of the Brillouin zone for greenalite. Tests using the computationally less demanding DFT method (without Hubbard U) showed that considering only one shifted q-point led to a relative uncertainty smaller than 3% on both the β and $\langle F \rangle$. The same linear response calculations provided the average force constant $\langle F \rangle$ of each Fe crystallographic site. This quantity corresponds to the harmonic restoring force constants, along the three orthogonal directions, that tend to pull back the studied atom in its equilibrium position. and can be calculated from the linear response method. This method was also used for instance in Aarons et al.[104] and Dauphas et al.[105]. All cell parameters from models are detailed in Table 1, and the experimental data used to validate the model results for greenalite and ferrihydrite were taken from Gruner (1936)[106] and Michel et al. (2007)[91] respectively

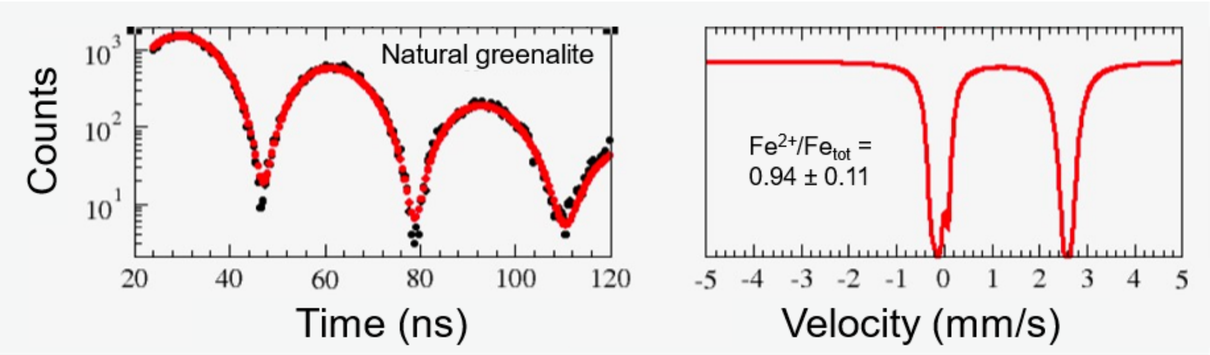

Figure 5. Left: Time domain synchrotron Mössbauer spectra (SMS) of natural greenalite standard left column. **Right:** Corresponding simulated energy domain spectra presented in the more familiar Doppler velocity shift units. The isomer shifts are relative to the Fe^{3+} component which is set to zero. The CONUSS program[9] was used for data evaluation and simulations. Estimated Fe redox states and associated errors are shown on the right-hand panels. The sample was determined to have $Fe^{2+}/Fe_{tot} = 0.94 \pm 0.11$.

3. RESULTS

3.1. Mineral characterization results

The XRD spectra obtained on the synthesized ferrihydrite samples (Figs. 4A-B) were consistent with those expected for 2-line and 6-line ferrihydrite, respectively[107]. From HR-TEM analysis, the lattice planes in SAED patterns agreed well with published data for 2-line and 6-line ferrihydrite (Figs. 4C-D)[79]. Images of 2-line ferrihydrite suggested crystallite sizes of ~2.5 nm, though the domain divisions were mostly indistinct. Images of 6-line ferrihydrite showed clearer domains of ~5 nm diameter. Fits to the forward-scattering spectrum for the natural greenalite standard using the CONUSS software[85] indicated ~94 % Fe^{2+} and ~6 % Fe^{3+} ($Fe^{2+}/Fe_{tot} = 0.94 \pm 0.11$; Table 2, Fig. 5). The statistically insignificant quantity of Fe^{3+} in this sample allows us to treat it as a ferrous endmember for NRIXS interpretations.

3.2. NRIXS and DFT + U *results*

The measured and calculated pDOS are provided in a spreadsheet as supplementary online materials, including the calculated pDOS for Fe in each of the three crystallographic sites in the modeled ferrihydrite. The polynomial expressions for β are given in Table 2, where we display the first three terms. The force constants for each mineral are also compiled in Table 2. NRIXS measurements and *ab initio* calculations yield the Fe pDOS (Fig. 6, Supplementary Material), $\langle F \rangle$ values (Figs. 7-8, Table 2), and β factors (using Eq. 2; Fig. 9, Table 2) in 2L-, 6L-ferrihydrite and greenalite. In the simulations, the DFT + U approach resulted in a relaxed structure that better fits experimental constraints on the crystallographic dimensions for Fe^{2+} greenalite ($Fe_3Si_2O_5(OH)_4$) than DFT alone, whilst for other minerals DFT + U and simpler DFT approaches gave similar levels of agreement with experiments (Table 1, Fig. 3). We thus report and focus our discussion of simulations on the DFT + U results. DFT based force constants (not reported) were shifted to lower force constant values by about 40 N/m compared to DFT + U. Because interpretations of natural isotopic variations rely on differences between β-factors between minerals and we do not mix results obtained from different methods, a constant shift in force constant does not affect the conclusions.

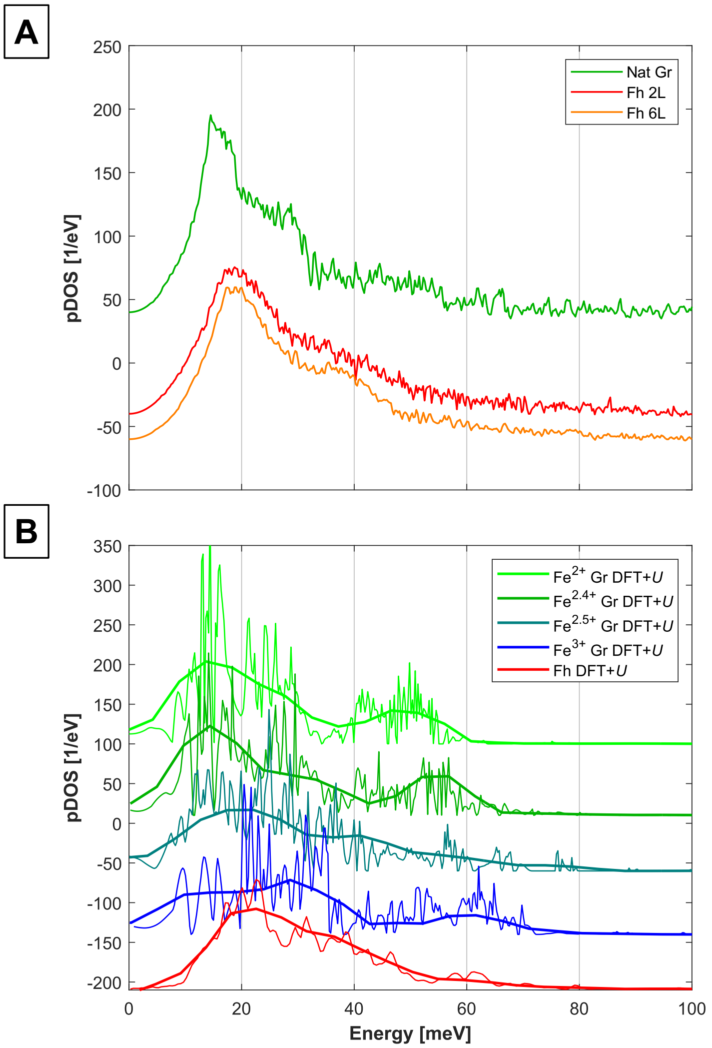

Figure 6. A: Average measured partial phonon density of states (pDOS) of iron in natural greenalite (Nat Gr) and laboratory synthesized ferrihydrite (Fh), determined by NRIXS analysis. **B:** Partial phonon density of states (pDOS) of iron in Fe^{2+}, $Fe^{2.4+}$ (vacancy substituted) $Fe^{2.5+}$ (Ferri-Tschermak substituted) and Fe^{3+} (vacancy substituted) greenalite (Gr), and ferrihydrite (Fh), determined by DFT+U simulations. Raw pDOS and pDOS smoothed for clarity of broad features are shown in lighter and heavier lines, respectively. All data are provided in a spreadsheet as supplementary online materials. pDOS curves are arbitrarily shifted on the vertical axis to improve readability in **A** and **B**, with increasingly oxidized materials shown lower in the vertical order.

Table 2. Polynomial fits for $1000\ln\beta = A_1X + A_2X^2 + A_3X^3$, with $X = 10^6/T^2$ (T in K), and force constants, $\langle F \rangle$, for Fe in greenalite and ferrihydrite. Error bars show the 95 % confidence interval on NRIXS determinations, and 3% estimated relative uncertainty on $\langle F \rangle$ values determined via DFT + *U* based on uncertainties in vibrational frequencies.

	A_1	**A_2**	**A_3**	**$\langle F \rangle$ (N m^{-1})**
DFT + *U*				
Fe^{2+} Greenalite	$6.12\times10^{-1} \pm 1.84\times10^{-2}$	$-2.75\times10^{-3} \pm 8.25\times10^{-5}$	$2.13\times10^{-5} \pm 6.39\times10^{-7}$	214 ± 6
$Fe^{2.4+}$ Greenalite (octahedral vacancy)	$7.04\times10^{-1} \pm 2.11\times10^{-2}$	$-3.97\times10^{-3} \pm 1.19\times10^{-4}$	$3.70\times10^{-5} \pm 1.11\times10^{-6}$	243 ± 7
$Fe^{2.5+}$ Greenalite (ferri-Tschermak)	$6.79\times10^{-1} \pm 2.04\times10^{-2}$	$-4.02\times10^{-3} \pm 1.21\times10^{-4}$	$4.37\times10^{-5} \pm 1.31\times10^{-6}$	238 ± 7
Fe^{3+} Greenalite	$8.42\times10^{-1} \pm 2.53\times10^{-2}$	$-5.73\times10^{-3} \pm 1.72\times10^{-4}$	$5.94\times10^{-5} \pm 1.78\times10^{-6}$	295 ± 9
Ferrihydrite	$7.08\times10^{-1} \pm 2.12\times10^{-2}$	$-3.84\times10^{-3} \pm 1.15\times10^{-4}$	$3.48\times10^{-5} \pm 1.04\times10^{-6}$	235 ± 7
NRIXS				
Natural Greenalite	$6.32\times10^{-1} \pm 8.2\times10^{-2}$	$-4.80\times10^{-3} \pm 1.79\times10^{-3}$	$1.06\times10^{-4} \pm 6.52\times10^{-5}$	222 ± 29
Ferrihydrite 2L	$7.31\times10^{-1} \pm 3.7\times10^{-2}$	$-4.71\times10^{-3} \pm 6.9\times10^{-4}$	$6.96\times10^{-5} \pm 2.47\times10^{-5}$	256 ± 13
Ferrihydrite 6L	$7.52\times10^{-1} \pm 3.7\times10^{-2}$	$-5.56\times10^{-3} \pm 8.5\times10^{-4}$	$1.19\times10^{-5} \pm 3.81\times10^{-5}$	263 ± 13
Ferrihydrite average	$7.41\times10^{-1} \pm 2.6\times10^{-2}$	$-5.04\times10^{-3} \pm 5.4\times10^{-4}$	$8.44\times10^{-5} \pm 2.07\times10^{-5}$	260 ± 9

The pDOSs calculated from NRIXS data (Fig. 6A) lack sharp features seen in DFT + *U* calculations. This is not likely due to the finite energy resolution of the monochromator because SciPhon implements an iterative procedure to deconvolve the energy resolution function from the measured spectrum[84]. A more plausible explanation is that it is due to the fine-grained or amorphous nature of the targeted powder samples.

3.2.1. Greenalite $\langle F \rangle$ values and pDOS

The DFT+U calculations produced $\langle F \rangle$ values of 214 ± 6, 243 ± 7, and 295 ± 9 N m^{-1} for Fe^{2+}, Fe$^{2.4+}$, and Fe^{3+} greenalite, and 238 ± 7, for Fe$^{2.5+}$ cronstedtite, respectively (Figs. 7-8, Table 2). There is a very strong (R^2 = 0.9977) negative correlation between Fe^{2+}/Fe$_{tot}$ and $\langle F \rangle$ in the simulated greenalites suggesting that Fe valence state is the sole control on $\langle F \rangle$ in this mineral (Fig. 7). Meanwhile, the Fe$^{2.5+}$ cronstedtite falls off of this trendline, likely reflecting the different average bonding environment for Fe in this structure with Fe in both octahedral and tetrahedral sites (Fig. 3C). For the natural (ferrous) greenalite standard, we calculated $\langle F \rangle$ = 222 ± 29 N m^{-1} using S(E) from NRIXS (Figs. 7-8, Table 2).

3.2.2. Ferrihydrite $\langle F \rangle$ values and pDOS

The DFT + U for ferrihydrite (Fe_5O_8H) gave a $\langle F \rangle$ value of 235 ± 7 Nm^{-1}. For the NRIXS analysis of experimentally synthesized ferrihydrite, we present a weighted average $\langle F \rangle$ value of 260 ± 9 N m^{-1}, as the values for 2-line and 6-line ferrihydrite were identical within error (Figs. 7-8, Table 2). The pDOS determined for both ferrihydrite structures via NRIXS compared favorably, both in terms of shape and position of the energy peak, with the pDOS determined from the DFT + U ferrihydrite model.

3.2.3. Comparison of $\langle F \rangle$ values in greenalite and ferrihydrite

Both DFT + U and NRIXS results showed that Fe^{2+}-greenalite has a lower Fe force constant than ferrihydrite and should thus impart a lighter Fe isotopic composition than ferrihydrite at equilibrium. DFT + U results indicate that mixed-valence forms of greenalite and cronstedtite have Fe force constants similar to ferrihydrite and consequently may have similar Fe isotopic compositions to ferrihydrite at equilibrium. From DFT + U, the $\langle F \rangle$ value of ferrihydrite is 21 N m^{-1} higher than that of Fe^{2+}-greenalite, and identical within error to that of Fe$^{2.4+}$ greenalite and Fe$^{2.5+}$ cronstedtite (Fig. 7).

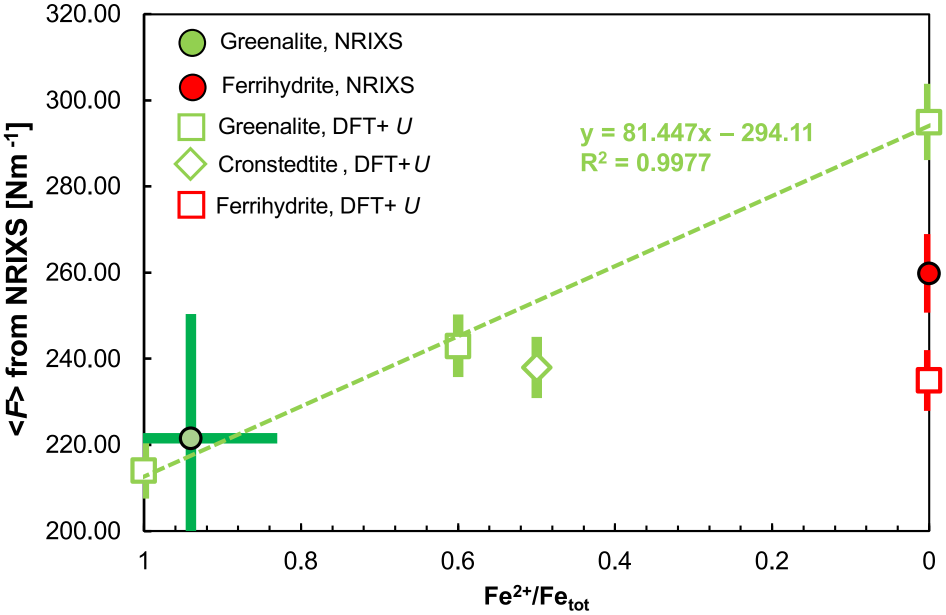

Figure 7. Force constant ($\langle F\rangle$) of greenalite and ferrihydrite, *vs*. Fe^{2+} content as a proportion of total Fe (Fe$_{tot}$). Filled circles show $\langle F\rangle$ for the natural greenalite standard (green) and the error weighted average of 2-line and 6-line ferrihydrite (red) from NRIXS analyses. Open squares show $\langle F\rangle$ for greenalite (green) and ferrihydrite (red) from DFT + U calculations (right-hand axis). Open green diamond shows $\langle F\rangle$ for cronstedtite with a ferri-Tschermak substitution. The green dashed line shows the linear correlation between Fe valence state and $\langle F\rangle$ in modeled greenalites (not including cronstedtite). Error bars show the 95 % confidence interval on NRIXS determinations, and 3% relative uncertainty on $\langle F\rangle$ values determined via DFT + U.

3.2.4. Discrepancy between DFT + U *and NRIXS determinations of* $\langle F\rangle$

The $\langle F\rangle$ of Fe^{3+} in ferrihydrite determined from DFT + U simulations is ~25 N m^{-1} lower than the average value determined from NRIXS. This offset is similar to that observed between DFT + U calculations and NRIXS determinations of $\langle F\rangle$ for goethite[62] and larger than the one previously observed for hematite[63] (Fig. 8). It should also be noted here that the DFT + U results for ferrihydrite (using Michel[91] model) and goethite[62] have similar Fe force constants that overlap within error, and it is thus expected that the Drits[92] model ferrihydrite, which is more similar to the Michel model ferrihydrite than it is to goethite, would fall within this range as well. For natural Fe^{2+} greenalite, the $\langle F \rangle$ determined via NRIXS agreed within the 95% confidence interval with the calculated based on DFT + U. All data from this study, along with previous goethite and hematite data[62,63], are consistent within error with an average 16 N m^{-1} offset to higher values in NRIXS vs. DFT + U determinations of $\langle F \rangle$ (Fig. 8). Due to the offset between *ab initio* and NRIXS determinations of $\langle F \rangle$, below we only consider Fe isotopic fractionations between ferrihydrite and greenalite determined via a single method (NRIXS or DFT + U) rather than mixing outputs from different approaches.

3.2.5. Equilibrium iron isotopic fractionations between ferrihydrite and greenalite

We describe Fe isotopic fractionations in terms of 1000lnα values (where we consider the $^{56}Fe/^{54}Fe$ ratio), using β factors calculated from the three-term polynomial expansion at 22 °C (Table 2), to enable comparison to previous experimental work, and present fractionations on the familiar $\delta^{56}Fe$ scale. We define the following abbreviations for the phases used in calculating α values: Fh – ferrihydrite; Gr2+ – reduced or ferrous greenalite, represented by the modeled Fe^{2+} endmember and the natural ferrous greenalite standard, in DFT + U and NRIXS determinations, respectively; Gr2.4+ – mixed valence greenalite, represented by the modeled $Fe^{2.4+}$ structure in DFT + U; and Gr3+ – oxidized greenalite, represented by the modeled Fe^{3+} endmember in DFT + U. We focus our discussion and interpretations on the greenalites with all Fe in octahedral sites and Fe^{3+} accompanied by vacancy substitution, because Mössbauer studies indicate that this is the site where Fe^{3+} substitution takes place in naturally occurring greenalite[88]. Results for the cronstedtitetype model are displayed in figures but are not discussed at length below in reference to the Fe isotopic record of IFs.

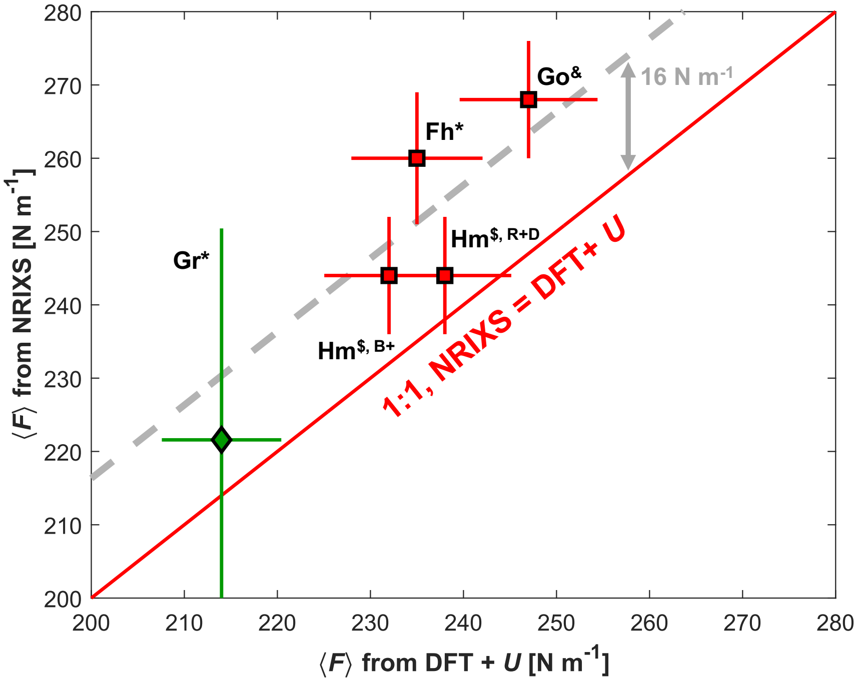

Figure 8. Intercomparison of force constants ⟨*F*⟩ data from NRIXS and *ab initio* DFT+*U* simulations for natural greenalite (Gr), ferrihydrite (Fh), goethite (Go), and hematite (Hm), from this study and literature. Greenalite is displayed as a green diamond, and ferric (oxyhydr)oxides are displayed as red squares. The black dotted line is a slope 1:1 line where data would fall if there was perfect agreement between the two techniques. The grey dashed line shows a slope 1 line that minimizes error-weighted deviations of the datapoints and indicates a ~16 N m^{-1} offset to higher values in NRIXS determinations versus DFT + *U* determinations of ⟨*F*⟩ that is similar to that observed in previous studies of ferric (oxyhydr)oxide minerals (Blanchard et al., 2015; Dauphas et al., 2012). Error bars show the 95 % confidence interval on NRIXS determinations, and 3% relative uncertainty on ⟨*F*⟩ values determined via DFT + *U*. Superscripts: * NRIXS and DFT+*U* data from this study; & NRIXS and DFT+*U* data from Blanchard et al. (2015); $ NRIXS data from Dauphas et al. (2012); B+ DFT+*U* data from Blanchard et al. (2009); R+D DFT data from Rustad and Dixon (2009).

From DFT + *U*, $1000\ln\alpha_{\text{Fh-Gr2+}} = +0.98 \pm 0.31$ ‰ and from NRIXS, $1000\ln\alpha_{\text{Fh-Gr2+}} = 1.19 \pm 1.34$ ‰ (Fig. 9). Most of the uncertainty in this case results from the less precise NRIXS-derived force constant for natural greenalite. These results agree very well in indicating a ~1 ‰ equilibrium Fe isotopic fractionation between ferrihydrite and ferrous greenalite, favoring higher $^{56}Fe/^{54}Fe$ in ferrihydrite. From DFT + *U*, $1000\ln\alpha_{Fh\text{-}Gr2.4+} = +0.06 \pm 0.32$ ‰ (Fig. 9). These data suggest that the equilibrium fractionation between mixed valence greenalite compositions and ferrihydrite could be small compared to many low temperature fractionations typically observed between species with different Fe redox states. Last, from DFT+*U*, $1000\ln\alpha_{Fh\text{-}Gr3+} = -1.32 \pm 0.36$ ‰ (Fig. 9). This result indicates that an Fe^{3+} endmember of greenalite should be significantly isotopically heavier than coexisting ferrihydrite and other HFOs, which might also predict that naturally occurring hisingerite, which is structurally similar to our modeled endmember, may take on a very heavy Fe isotopic composition during its formation during serpentinization of ferroan peridotites[90].

4. DISCUSSION

4.1. Predicting equilibrium iron isotopic fractionations during greenalite precipitation

Fluid-mineral equilibration experiments have consistently resulted in $1000\ln\alpha_{Ferrihydrite\text{-}Fe(II)aq}$, $1000\ln\alpha_{Hematite\text{-}Fe(II)aq}$, and $1000\ln\alpha_{Fe(III)\text{-}Fe(IIaq)}$ values on the order of +3.0 – 3.2 ‰ for $\delta^{56}Fe$[58,59,66] at around 22 °C (Fig 10). These results indicate that i) the fractionation during ferric oxide equilibration with an Fe^{2+} solution is dominated by the equilibrium fractionation between $Fe(II)_{aq}$ and $Fe(III)_{aq}$[59], and ii) the equilibrium fractionation between ferric oxides and aqueous Fe(III) is small[58]. An outlier among this class of experiments is the finding of a ~1 ‰ fractionation between Fe(II) and goethite[55]. However, similar force constants were found for ferrihydrite and goethite in this study and that of Blanchard et al.[62], with goethite having a slightly (~10 Nm^{-1}) higher value of $\langle F \rangle$ in both DFT+*U* and NRIXS datasets, which draws the small $1000\ln\alpha_{Goethite\text{-}Fe(II)aq}$ determinations into question. Surface exchange effects were a complicating factor in interpreting the equilibration experiments of Beard et al.[55] and these might have impacted the net fractionation during goethite formation while obscuring the equilibrium value of 1000ln$\alpha_{\text{Goethite-Fe(II)aq}}$.

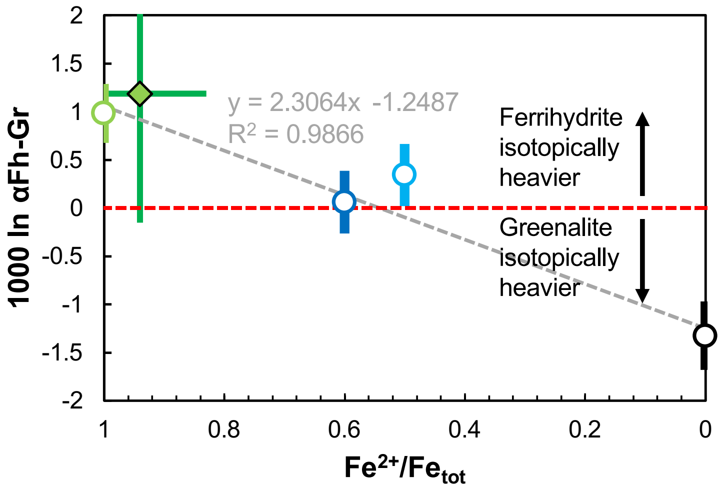

Figure 9. Equilibrium Fe isotopic fractionations between ferrihydrite and greenalite materials determined in this study, expressed as 1000 ln$\alpha_{\text{Fh-Gr}}$ for the ^{56}Fe/^{54}Fe ratio, where a positive value indicates relative enrichment of heavy Fe isotopes in ferrihydrite. Different symbols show 1000 ln$\alpha_{\text{Fh-Gr}}$ at 22 °C for different greenalite materials and analytical techniques as follows: natural greenalite standard (NRIXS) –filled green diamond; ferrous greenalite via DFT + *U* – open pale green circle; $Fe^{2.4+}$ greenalite via DFT + *U* – open dark blue circle; $Fe^{2.5+}$ cronstedtite via DFT + *U* – open pale blue circle; Fe^{3+} greenalite via DFT + *U* – open black circle. The grey dashed line shows the linear correlation between Fe valence state and 1000 ln$\alpha_{\text{Fh-Gr}}$ in modeled greenalites (not including the $Fe^{2.5+}$ cronstedtite). Error bars show the 95 % confidence interval on NRIXS determinations, and 3% relative uncertainty on $\langle F \rangle$ values determined via DFT + *U*.

We take 1000ln$\alpha_{\text{Fh-Fe(II)aq}}$ = +3.0 ‰ as a representative value for the equilibrium fractionation between ferrihydrite and aqueous Fe(II) for anchoring to ferrihydrite-mineral pairs. Equilibrium Fe isotopic fractionations between greenalite and aqueous Fe(II) can then be calculated as 1000ln$\alpha_{\text{Fh-Fe(II)aq}}$ − 1000ln$\alpha_{\text{Fh-Greenalite}}$. For ferrous greenalite, we find 1000ln$\alpha_{\text{Gr2+-Fe(II)aq}}$ = +2.02 ± 0.31 ‰ (DFT + *U*) and +1.81 ± 1.34 ‰ (NRIXS) (Fig. 10). For mixed valence greenalite, we find 1000ln$\alpha_{\text{Gr2.4+-Fe(II)aq}}$ = +2.94 ± 0.32 ‰ (DFT+*U*; Fe^{2+}/Fe_{tot} = 0.40) (Fig. 10). For ferric greenalite/hisingerite we find 1000ln$\alpha_{\text{Gr3+-Fe(II)aq}}$ = +4.3 ± 0.36 ‰ (DFT + *U*) (Fig. 10).

Experimental studies to constrain the Fe isotopic fractionation during unidirectional $Fe(II)_{aq}$ oxidation and HFO precipitation via various oxidation mechanisms produce much smaller Fe isotopic fractionations between ferrous iron solutions and ferric precipitates, resulting in values of $1000\ln\alpha_{HFO\text{-}Fe(II)aq}$ = 1.5 ‰ (anoxygenic photosynthesis)[57], 1.2 ‰ (UV photooxidation)[20], and 1.0 ‰ (air/O_2)[56] (Fig. 10). The reason for these smaller fractionations compared to fluid-mineral equilibration experiments is likely that during unidirectional Fe^{2+} oxidation and HFO precipitation, full equilibrium between the precipitate and fluid pools is not reached; even though the results of at least some of these experiments follow the high-temperature limit equilibrium mass fractionation law[20]. Anchoring greenalite-ferrihydrite mineral pairs to these smaller $1000\ln\alpha_{HFO\text{-}Fe(II)aq}$ values for unidirectional oxidation and precipitation would result in considerably smaller fractionations for greenalite precipitation. For example we would find $1000\ln\alpha_{Gr2+\text{-}Fe(II)aq}$ ~ -0.2 to +0.5 ‰, $1000\ln\alpha_{Gr2.4+\text{-}Fe(II)aq}$ ~ +0.9 to +1.4 ‰ and $1000\ln\alpha_{Gr3+\text{-}Fe(II)aq}$ ~ +2.3 to +2.8 ‰ (Fig. 10), depending on the specific experiment used for anchoring.

4.2. Implications for the origins of Archean iron formations

The fractionations calculated from DFT + *U* and NRIXS measurements can be used to address the Fe isotopic imprint of potential primary greenalite precipitates. We find that equilibrium Fe isotopic fractionation between a representative HFO precursor for IFs and ferrous greenalite is on the order of 1–1.2 ‰ for $^{56}Fe/^{54}Fe$ at 22°C, with ferrihydrite being relatively enriched in ^{56}Fe. This result is consistent between DFT+*U* and NRIXS determinations.

Depending on whether ferrihydrite-greenalite fractionation is anchored to ‘exchange/equilibration’ or ‘unidirectional/precipitation’-style experiments, we can infer fractionations accompanying the precipitation of ferrous greenalite that range from a ~2 ‰ enrichment in δ^{56}Fe relative to the marine reservoir to a slightly negative or no fractionation, respectively (Fig. 10). The latter result would immediately rule out a pure ferrous greenalite precursor for IFs (Fig. 10). However, it is not clear that anchoring to unidirectional ferrihydrite precipitation experiments is an appropriate assumption when calculating the pure equilibrium fractionation involved in greenalite precipitation. Therefore, below we expand upon the discussion of fractionations anchored to the +3.0 ‰ exchange/equilibrium class of experiments and the implications of the largest possible equilibrium fractionations that may be associated with Fe^{2+} greenalite.

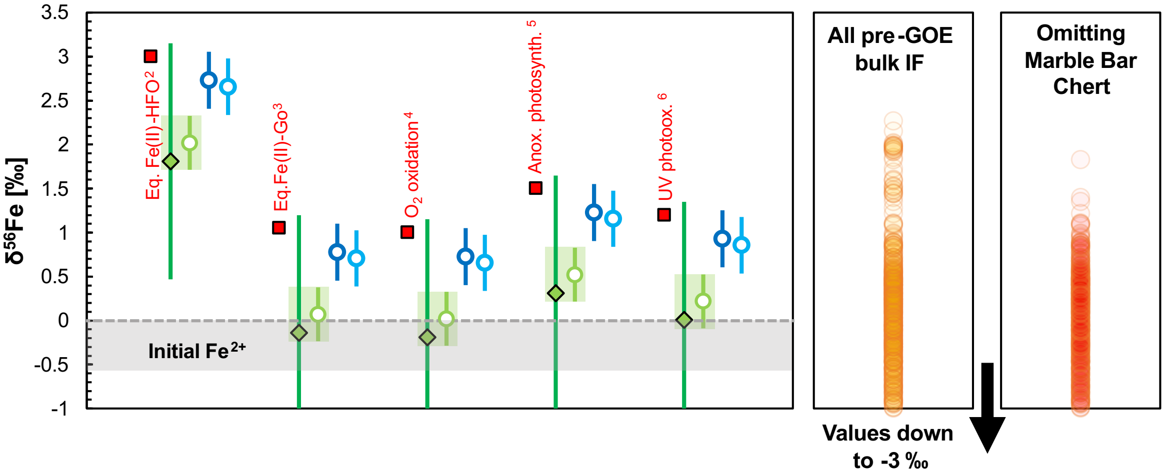

Figure 10. Left: Range of possible initial Fe isotopic fractionations during greenalite precipitation determined by anchoring greenalite-ferrihydrite mineral pairs to published fractionations between aqueous Fe(II) at δ^{56}Fe = 0 ‰ and hydrous ferric oxide (HFO) determined in different experimental studies (red squares). Symbols showing the fractionation in the greenalite-ferrihydrite mineral pair at 22 °C are the same as those in Fig. 9. Error bars show the 95 % confidence interval on NRIXS determinations, and 3% relative uncertainty on $\langle F \rangle$ values determined via DFT + U. Green shaded boxes show the range of fractionations for Fe^{2+} greenalite allowed within the error range of both techniques. Superscripts: [1]Heard and Dauphas (2020); [2]Wu et al. (2011); [3]Beard et al. (2010); [4]Bullen et al. (2001); [5]Croal et al. (2004); [6]Nie et al. (2017). Right: Range of δ^{56}Fe observed in pre-GOE IFs for comparison to greenalite fractionations, compiled by Heard and Dauphas (2020). Compilations are shown with (orange, left) and without (red, right) the Marble Bar Chert, which contains the highest δ^{56}Fe values in this record but which may not record primary depositional signatures due to extensive alteration (Rasmussen et al., 2014; Rasmussen and Muhling 2022).

Our results show that the maximum possible value for $1000\ln\alpha_{\mathrm{Gr2+\text{-}Fe(II)aq}}$ is +2.02 ± 0.31 ‰ (DFT + *U*) or +1.81 ± 1.34 ‰ (NRIXS) (Fig. 10), with the largest value allowable within the error bar of both techniques being +2.3 ‰ (Fig. 10). If a hydrothermal Fe^{2+} source to the Archean oceans had $\delta^{56}Fe = 0$, towards the higher end of values for Fe^{2+} inputs to the modern oceans [108,109], IFs with $\delta^{56}Fe$ values as high as 2.3 ‰ could therefore be explainable by low degrees of partial Fe^{2+} greenalite precipitation at equilibrium. Kinetic isotope effects associated with oversaturation of a greenalite precursor mineral in solution would potentially decrease this positive fractionation, and further experiments will need to address this, as discussed in Section 5.

We compare these inferred fractionations to the pre-GOE bulk rock $\delta^{56}Fe$ record of IFs, which should ideally be unaffected by closed-system inter-mineral fractionation and may represent primary Fe depositional fluxes. As shown in Figure 10, the inferred value for $1000\ln\alpha_{\mathrm{Gr2+\text{-}Fe(II)aq}}$ can account for the Fe isotopic composition of all pre-GOE bulk IF material except the 3.4 Ga Marble Bar Chert, which has $\delta^{56}Fe$ values as high as 2.6 ‰. At face value, the inability of Fe^{2+} greenalite to reproduce the $\delta^{56}Fe$ of such an ancient example of IF material is significant, because a larger fractionation would require an Fe^{3+}-bearing precipitate and necessitate the occurrence of marine Fe^{2+} oxidation since at least 3.4 Ga.

The Marble Bar Chert does, however, reach considerably higher $\delta^{56}Fe$ values than other pre-GOE bulk IFs, which, outside of a single outlying value, are < 1.7 ‰ (Fig. 10). We cannot definitively determine if the high $\delta^{56}Fe$ values of the Marble Bar Chert reflect atypical depositional processes (for the Archean) or secondary alteration processes that enriched the bulk rock in heavy Fe isotopes relative to the initial precipitate. Microscale petrographic studies of these rocks have revealed that fine grained hematite originally thought to be primary[61,110], may instead be an alteration product of primary greenalite[41,43]. Oxidative alteration would not be expected to reset bulk Fe isotopic compositions in an IF, given the decreased fluid mobility of Fe^{3+} relative to Fe^{2+}. A previous study showed indeed that primary signatures should be retained in bulk δ^{56}Fe values through high grade metamorphism even without net oxidation[49]. One possible reason why the Marble Bar Chert has uniquely high δ^{56}Fe relative to other Archean IFs may be its low Fe content ($[Fe_2O_3] < 10$ wt %) that strictly characterizes it as a jaspilite. With lower Fe contents, they may have been less strongly rock-buffered during fluid flow and more susceptible to isotopic overprinting. This low Fe content alone suggests the Marble Bar Chert is unrepresentative of the general pre-GOE IF record we aim to compare to isotopic systematics of greenalite. We cannot conclusively rule out the elevated δ^{56}Fe of the Marble Bar Chert as evidence for non-zero levels of Fe^{2+} oxidation as early as 3.4 Ga, but context suggests that this single formation should not be given too much weight in understanding the early marine Fe cycle.

It is apparent from the results of this study that Fe isotope systematics alone cannot provide a constraint on the primary mineralogy of IFs; however, reconciling our data with the rock record suggests that partial Fe^{2+} oxidation is more consistent with the Fe isotopic record and measurements of early-preserved IF greenalite than pure ferrous greenalite. The DFT + U simulations indicate that greenalite with an average Fe valence state of 2.4+ should impart essentially identical equilibrium Fe isotopic systematics to ferrihydrite. This valence state is intriguing because IFs themselves have an average Fe valence state of 2.4+[16]. However, synchrotron-based analyses of well-preserved pre-GOE IFs suggest that greenalite typically has lower Fe^{3+} contents ($Fe^{3+}/Fe_{tot} \approx 0.1\text{-}0.2$)[39]. Using the relationship between Fe valence state and $1000\ln\alpha_{Fh\text{-}Gr}$ from our DFT + *U* simulations (Fig. 9), we can predict that greenalites with the recorded range of Fe^{3+} contents would form 0.6-0.8 ‰ per mil lighter than ferrihydrite, allowing $1000\ln\alpha_{Gr\text{-}Fe(II)aq}$ values up to 2.2-2.4 ‰ that account for the entire pre-GOE IF record save for a few values in the anomalous Marble Bar Chert[61]. Therefore, it is possible that a relatively low-Fe^{3+} greenalite precursor for pre-GOE IFs may be reconciled with the $\delta^{56}Fe$ record even if the most extreme outlier values are indeed primary depositional signatures.

5. FUTURE DIRECTIONS

The uncertainty in predicted greenalite-$Fe(II)_{(aq)}$ Fe isotopic fractionations, stemming predominantly from uncertainty in which HFO-$Fe(II)_{(aq)}$ fractionation factors to anchor to, underlines the importance of future experimental works to determine the Fe isotopic fractionation during unidirectional greenalite precipitation from ferrous solutions. Unidirectional greenalite (or greenalite precursor mineral) precipitation experiments should provide a more refined picture of Fe isotopic fractionation associated with natural greenalite formation. In particular, experiments should be conducted with solutions containing both Fe^{2+} and Mn^{2+}. By coupling $\delta^{56}Fe$ measurements with measurements of Mn/Fe in co-sampled solutions and greenalite precursor precipitates, the chemical evolution of solutions and precipitates could be compared to the well-established negative correlation seen in ln(Mn/Fe) *vs*. $\delta^{56}Fe$ plots of IFs of all ages[111–115]. This negative correlation is well-explained by preferential incorporation of Fe into IF precipitates relative to Mn, because the latter requires higher redox potentials to be oxidized to insoluble Mn^{4+} hydroxides[113]. Meanwhile, Fe^{2+} and Mn^{2+} have very similar geochemical behaviors, so the degree of incorporation of Mn in Fe^{2+}-greenalite and mixed valence greenalite precursor material will offer a useful second variable to disentangle the surprisingly similar δ^{56}Fe systematics of HFOs and Fe^{3+}-bearing greenalite.

Lastly, our finding that the Fe isotope record could be consistent with a role for greenalite rather than HFOs as a dominant IF precursor has implications for understanding nutrient availability in the oceans in deep time, particularly prior to the GOE[33–38]. If a dominant HFO precursor for IF is not a necessity for ancient ocean chemistry models, it may not be appropriate to quantitatively reconstruct seawater nutrient concentrations using calibrations to HFO adsorption experiments. It is thus vital that future experimental studies into the precipitation of greenalite precursor material should include an exploration of the adsorption and coprecipitation of P, Ni, and other nutrient elements of interest onto these phases in seawater solutions. Having a more complete understanding of the range of dissolved [P] levels in the Archean oceans, in particular, may be vital for assessing the role that nutrient limitation and global rates of photosynthetic primary productivity played in the eventual rise of atmospheric O_2[37,116–118].

6. CONCLUSIONS

Assumptions about the primary mineralogy of IFs and iron-rich cherts deposited before the GOE underpin many aspects of early ocean chemical models. The canonical assumption that HFOs like ferrihydrite were the dominant precursor minerals in marine chemical sediments informs a view of the Archean defined by shallow oceans supporting the oxidation of dissolved Fe^{2+}, possibly as a direct or indirect effect of bacterial photosynthesis. The HFO model is also the foundation for several nutrient reconstructions for the early oceans, which are then interpreted in the context of biological drivers of changes in ocean and atmospheric oxygenation. An alternative model for pre-

GOE IFs and related sediments, informed by detailed petrography, posits that dominantly ferrous authigenic silicates like greenalite were the primary IF precursor mineral. This model was not testable with widely available Fe isotopic data for IFs because of a lack of constraints on the Fe isotopic systematics of greenalite.

Here, we determined the Fe force constant ($\langle F \rangle$) and Fe isotope β factors (which determine equilibrium Fe isotopic fractionation between phases) for greenalite and ferrihydrite, using DFT+*U ab initio* calculations and NRIXS analysis of natural and laboratory synthesized minerals. Our results indicate that $1000\ln\alpha_{\text{Fh-Gr2+}} = +0.98 \pm 0.31$ ‰ (DFT + *U*) and 1.19 ± 1.34 ‰ (NRIXS), $1000\ln\alpha_{\text{Fh-Gr2.4+}} = +0.06 \pm 0.32$ ‰ (DFT + *U*), and $1000\ln\alpha_{\text{Fh-GrOx}} = -1.32 \pm 0.36$ ‰ (DFT + *U*), where the modeled oxidized greenalite endmember may provide an estimate of the Fe isotopic systematics for the naturally-occurring mineral hisingerite.

By anchoring these results for fractionations in the greenalite-ferrihydrite mineral pair to published experimental data on the fractionation of δ^{56}Fe between HFOs and dissolved Fe^{2+}, we find that ferrous greenalite should, at equilibrium, precipitate with δ^{56}Fe fractionated either ~+2 ‰, or between -0.2 and +0.5 ‰, relative to dissolved Fe^{2+}, depending on if calculated fractionations were tied to HFO-$Fe(II)_{aq}$ equilibration experiments or unidirectional $Fe(II)_{aq}$ oxidation and HFO precipitation experiments, respectively.

This dataset shows that a pathway to reconcile a greenalite-dominated IF depositional flux with the pre-GOE δ^{56}Fe IF record does exist, provided that either the most uniquely isotopically enriched pre-GOE IF material does not retain a representative primary depositional signal; or if precipitated greenalite had at least a few tens of % Fe^{3+} content due to Fe^{2+} oxidation process in the early oceans. The second of these results ties to the finding of this study that mixed-valence greenalite should form with similar Fe isotopic compositions to ferrihydrite and is also consistent with synchrotron-based determinations of low tens of % Fe^{3+} in IF greenalite. Because some form of the greenalite hypothesis appears to be a viable alternative to the HFO model to explain the Fe isotopic record of IFs, quantitative reconstructions of nutrient elements concentrations like [P] and [Ni] in the pre-GOE oceans based on HFO adsorption experiments should be viewed with caution. Comparable experiments featuring authigenic silicate phases like greenalite should be carried out, along with a variety of further experimental studies on the geochemical and isotopic systematics of these phases.

ACKNOWLEDGEMENTS

Work at the University of Chicago was funded by NASA grants 80NSSC17K0744 to ND and AWH (Habitable Worlds), 359NNX17AE86G (LARS), NNX17AE87G and 80NSSC20K0821 (Emerging Worlds), 80NSSC20K1409 (Habitable Worlds) to ND, 80NSSC18K1060 (Exobiology) to JEJ, NSF grant EAR-2001098 (CSEDI) to ND, and a DOE grant to ND. AWH acknowledges support from an Eckhardt Scholarship from the University of Chicago, a Crosby Postdoctoral Fellowship from Woods Hole Oceanographic Institution, and an Agouron Institute postdoctoral fellowship in geobiology. DFT calculations were performed using HPC resources from CALMIP (Grant 2021-P1037). This research used resources of the Advanced Photon Source, a U.S. Department of Energy (DOE) Office of Science user facility at Argonne National Laboratory and is based on research supported by the U.S. DOE Office of Science-Basic Energy Sciences, under

Contract No. DE-AC02-06CH11357. Discussions with Andrey Bekker and Chad Ostrander were appreciated.

Supplementary Information

- Details of laboratory synthesis, characterization, and NRIXS analysis of a hydrous silicate material intended to be a greenalite precursor phase.
- Tables containing: full NRIXS analysis results in the form of SciPhon outputs (Table S1); $\langle F \rangle$ values and polynomial fits to $1000\ln\beta = A_1X + A_2X^2 + A_3X^3$ for experimentally synthesized material analyzed via NRIXS (Table S2) ; and atomic positions for all mineral structures modeled in DFT + U simulations (Table S3).

REFERENCES

(1) Bekker, A.; Holland, H. D.; Wang, P.-L.; Rumble Iii, D.; Stein, H. J.; Hannah, J. L.; Coetzee, L. L.; Beukes, N. J. Dating the Rise of Atmospheric Oxygen. *Nature* **2004**, *427* (6970), 117–120. https://doi.org/10.1038/nature02260.

(2) Gumsley, A. P.; Chamberlain, K. R.; Bleeker, W.; Söderlund, U.; Kock, M. O. de; Larsson, E. R.; Bekker, A. Timing and Tempo of the Great Oxidation Event. *Proc. Natl. Acad. Sci.* **2017**, *114* (8), 1811–1816. https://doi.org/10.1073/pnas.1608824114.

(3) Poulton, S. W.; Bekker, A.; Cumming, V. M.; Zerkle, A. L.; Canfield, D. E.; Johnston, D. T. A 200-Million-Year Delay in Permanent Atmospheric Oxygenation. *Nature* **2021**, 1–5. https://doi.org/10.1038/s41586-021-03393-7.

(4) Poulton, S. W.; Canfield, D. E. Ferruginous Conditions: A Dominant Feature of the Ocean through Earth’s History. *Elements* **2011**, *7* (2), 107–112. https://doi.org/10.2113/gselements.7.2.107.

(5) Derry, L. A.; Jacobsen, S. B. The Chemical Evolution of Precambrian Seawater: Evidence from REEs in Banded Iron Formations. *Geochim. Cosmochim. Acta* **1990**, *54* (11), 2965–2977. https://doi.org/10.1016/0016-7037(90)90114-Z.

(6) Holland, H. D. The Oceans; A Possible Source of Iron in Iron-Formations. *Econ. Geol.* **1973**, *68* (7), 1169–1172. https://doi.org/10.2113/gsecongeo.68.7.1169.

(7) Isley, A. E. Hydrothermal Plumes and the Delivery of Iron to Banded Iron Formation. *J. Geol.* **1995**, *103* (2), 169–185.

(8) Jacobsen, S. B.; Pimentel-Klose, M. R. Nd Isotopic Variations in Precambrian Banded Iron Formations. *Geophys. Res. Lett.* **1988**, *15* (4), 393–396. https://doi.org/10.1029/GL015i004p00393.

(9) Thompson, K. J.; Kenward, P. A.; Bauer, K. W.; Warchola, T.; Gauger, T.; Martinez, R.; Simister, R. L.; Michiels, C. C.; Llirós, M.; Reinhard, C. T.; Kappler, A.; Konhauser, K. O.; Crowe, S. A. Photoferrotrophy, Deposition of Banded Iron Formations, and Methane Production in Archean Oceans. *Sci. Adv.* **2019**, *5* (11), eaav2869. https://doi.org/10.1126/sciadv.aav2869.

(10) Alexander, B. W.; Bau, M.; Andersson, P.; Dulski, P. Continentally-Derived Solutes in Shallow Archean Seawater: Rare Earth Element and Nd Isotope Evidence in Iron Formation from the 2.9Ga Pongola Supergroup, South Africa. *Geochim. Cosmochim. Acta* **2008**, *72* (2), 378–394. https://doi.org/10.1016/j.gca.2007.10.028.

(11) Heard, A. W.; Aarons, S. M.; Hofmann, A.; He, X.; Ireland, T.; Bekker, A.; Qin, L.; Dauphas, N. Anoxic Continental Surface Weathering Recorded by the 2.95 Ga Denny Dalton Paleosol (Pongola Supergroup, South Africa). *Geochim. Cosmochim. Acta* **2021**, *295*, 1–23. https://doi.org/10.1016/j.gca.2020.12.005.

(12) Bekker, A.; Planavsky, N. J.; Krapež, B.; Rasmussen, B.; Hofmann, A.; Slack, J. F.; Rouxel, O. J.; Konhauser, K. O. 9.18 - Iron Formations: Their Origins and Implications for Ancient Seawater Chemistry. In *Treatise on Geochemistry (Second Edition)*; Holland, H. D., Turekian, K. K., Eds.; Elsevier: Oxford, 2014; pp 561–628. https://doi.org/10.1016/B978-0-08-095975-7.00719-1.

(13) Bekker, A.; Slack, J. F.; Planavsky, N.; Krapež, B.; Hofmann, A.; Konhauser, K. O.; Rouxel, O. J. Iron Formation: The Sedimentary Product of a Complex Interplay among Mantle, Tectonic, Oceanic, and Biospheric Processes. *Econ. Geol.* **2010**, *105* (3), 467–508. https://doi.org/10.2113/gsecongeo.105.3.467.

(14) Konhauser, K. O.; Planavsky, N. J.; Hardisty, D. S.; Robbins, L. J.; Warchola, T. J.; Haugaard, R.; Lalonde, S. V.; Partin, C. A.; Oonk, P. B. H.; Tsikos, H.; Lyons, T. W.; Bekker, A.; Johnson, C. M. Iron Formations: A Global Record of Neoarchaean to Palaeoproterozoic Environmental History. *Earth-Sci. Rev.* **2017**, *172*, 140–177. https://doi.org/10.1016/j.earscirev.2017.06.012.

(15) Trendall, A. F.; Morris, R. C. *Iron-Formation: Facts and Problems*; Elsevier, 2000.

(16) Klein, C. Some Precambrian Banded Iron-Formations (BIFs) from around the World: Their Age, Geologic Setting, Mineralogy, Metamorphism, Geochemistry, and Origins. *Am. Mineral.* **2005**, *90* (10), 1473–1499. https://doi.org/10.2138/am.2005.1871.

(17) Cloud, P. Paleoecological Significance of the Banded Iron-Formation. *Econ. Geol.* **1973**, *68* (7), 1135–1143. https://doi.org/10.2113/gsecongeo.68.7.1135.

(18) Braterman, P. S.; Cairns-Smith, A. G.; Sloper, R. W. Photo-Oxidation of Hydrated Fe2+—Significance for Banded Iron Formations. *Nature* **1983**, *303* (5913), 163–164. https://doi.org/10.1038/303163a0.

(19) Cairns-Smith, A. G. Precambrian Solution Photochemistry, Inverse Segregation, and Banded Iron Formations. *Nature* **1978**, *276* (5690), 807–808. https://doi.org/10.1038/276807a0.

(20) Nie, N. X.; Dauphas, N.; Greenwood, R. C. Iron and Oxygen Isotope Fractionation during Iron UV Photo-Oxidation: Implications for Early Earth and Mars. *Earth Planet. Sci. Lett.* **2017**, *458*, 179–191. https://doi.org/10.1016/j.epsl.2016.10.035.

(21) Kappler, A.; Pasquero, C.; Konhauser, K. O.; Newman, D. K. Deposition of Banded Iron Formations by Anoxygenic Phototrophic Fe(II)-Oxidizing Bacteria. *Geology* **2005**, *33* (11), 865–868. https://doi.org/10.1130/G21658.1.

(22) Konhauser, K. O.; Amskold, L.; Lalonde, S. V.; Posth, N. R.; Kappler, A.; Anbar, A. Decoupling Photochemical Fe(II) Oxidation from Shallow-Water BIF Deposition. *Earth Planet. Sci. Lett.* **2007**, *258* (1–2), 87–100. https://doi.org/10.1016/j.epsl.2007.03.026.

(23) Konhauser, K. O.; Hamade, T.; Raiswell, R.; Morris, R. C.; Ferris, F. G.; Southam, G.; Canfield, D. E. Could Bacteria Have Formed the Precambrian Banded Iron Formations? *Geology* **2002**, *30* (12), 1079–1082. https://doi.org/10.1130/0091-7613(2002)030<1079:CBHFTP>2.0.CO;2.

(24) Craddock, P. R.; Dauphas, N. Iron and Carbon Isotope Evidence for Microbial Iron Respiration throughout the Archean. *Earth Planet. Sci. Lett.* **2011**, *303* (1–2), 121–132. https://doi.org/10.1016/j.epsl.2010.12.045.

(25) Heimann, A.; Johnson, C. M.; Beard, B. L.; Valley, J. W.; Roden, E. E.; Spicuzza, M. J.; Beukes, N. J. Fe, C, and O Isotope Compositions of Banded Iron Formation Carbonates Demonstrate a Major Role for Dissimilatory Iron Reduction in ~2.5 Ga Marine Environments. *Earth Planet. Sci. Lett.* **2010**, *294* (1–2), 8–18. https://doi.org/10.1016/j.epsl.2010.02.015.

(26) Köhler, I.; Konhauser, K. O.; Papineau, D.; Bekker, A.; Kappler, A. Biological Carbon Precursor to Diagenetic Siderite with Spherical Structures in Iron Formations. *Nat. Commun.* **2013**, *4*, 1741. https://doi.org/10.1038/ncomms2770.

(27) Konhauser, K. O.; Newman, D. K.; Kappler, A. The Potential Significance of Microbial Fe(III) Reduction during Deposition of Precambrian Banded Iron Formations. *Geobiology* **2005**, *3* (3), 167–177. https://doi.org/10.1111/j.1472-4669.2005.00055.x.

(28) Walker, J. C. G. Suboxic Diagenesis in Banded Iron Formations. *Nature* **1984**, *309* (5966), 340–342. https://doi.org/10.1038/309340a0.

(29) Fischer, W. W.; Knoll, A. H. An Iron Shuttle for Deepwater Silica in Late Archean and Early Paleoproterozoic Iron Formation. *GSA Bull.* **2009**, *121* (1–2), 222–235. https://doi.org/10.1130/B26328.1.

(30) Nims, C.; Johnson, J. E. Exploring the Secondary Mineral Products Generated by Microbial Iron Respiration in Archean Ocean Simulations. *Geobiology* **2022**, *20* (6), 743–763. https://doi.org/10.1111/gbi.12523.

(31) Robbins, L. J.; Funk, S. P.; Flynn, S. L.; Warchola, T. J.; Li, Z.; Lalonde, S. V.; Rostron, B. J.; Smith, A. J. B.; Beukes, N. J.; Kock, M. O. de; Heaman, L. M.; Alessi, D. S.; Konhauser, K. O. Hydrogeological Constraints on the Formation of Palaeoproterozoic Banded Iron Formations. *Nat. Geosci.* **2019**, 1. https://doi.org/10.1038/s41561-019-0372-0.

(32) Dodd, M. S.; Papineau, D.; Pirajno, F.; Wan, Y.; Karhu, J. A. Minimal Biomass Deposition in Banded Iron Formations Inferred from Organic Matter and Clay Relationships. *Nat. Commun.* **2019**, *10* (1), 1–13. https://doi.org/10.1038/s41467-019-12975-z.

(33) Bjerrum, C. J.; Canfield, D. E. Ocean Productivity before about 1.9 Gyr Ago Limited by Phosphorus Adsorption onto Iron Oxides. *Nature* **2002**, *417* (6885), 159–162. https://doi.org/10.1038/417159a.

(34) Jones, C.; Nomosatryo, S.; Crowe, S. A.; Bjerrum, C. J.; Canfield, D. E. Iron Oxides, Divalent Cations, Silica, and the Early Earth Phosphorus Crisis. *Geology* **2015**, *43* (2), 135–138. https://doi.org/10.1130/G36044.1.

(35) Konhauser, K. O.; Robbins, L. J.; Pecoits, E.; Peacock, C.; Kappler, A.; Lalonde, S. V. The Archean Nickel Famine Revisited. *Astrobiology* **2015**, *15* (10), 804–815. https://doi.org/10.1089/ast.2015.1301.

(36) Konhauser, K. O.; Pecoits, E.; Lalonde, S. V.; Papineau, D.; Nisbet, E. G.; Barley, M. E.; Arndt, N. T.; Zahnle, K.; Kamber, B. S. Oceanic Nickel Depletion and a Methanogen Famine before the Great Oxidation Event. *Nature* **2009**, *458* (7239), 750–753. https://doi.org/10.1038/nature07858.

(37) Planavsky, N. J.; Rouxel, O. J.; Bekker, A.; Lalonde, S. V.; Konhauser, K. O.; Reinhard, C. T.; Lyons, T. W. The Evolution of the Marine Phosphate Reservoir. *Nature* **2010**, *467* (7319), 1088–1090. https://doi.org/10.1038/nature09485.

(38) Robbins, L. J.; Lalonde, S. V.; Planavsky, N. J.; Partin, C. A.; Reinhard, C. T.; Kendall, B.; Scott, C.; Hardisty, D. S.; Gill, B. C.; Alessi, D. S.; Dupont, C. L.; Saito, M. A.; Crowe, S. A.; Poulton, S. W.; Bekker, A.; Lyons, T. W.; Konhauser, K. O. Trace Elements at the Intersection of Marine Biological and Geochemical Evolution. *Earth-Sci. Rev.* **2016**, *163*, 323–348. https://doi.org/10.1016/j.earscirev.2016.10.013.

(39) Johnson, J. E.; Muhling, J. R.; Cosmidis, J.; Rasmussen, B.; Templeton, A. S. Low-Fe(III) Greenalite Was a Primary Mineral From Neoarchean Oceans. *Geophys. Res. Lett.* **2018**, *45* (7), 3182–3192. https://doi.org/10.1002/2017GL076311.

(40) Rasmussen, B.; Muhling, J. R.; Krapež, B. Greenalite and Its Role in the Genesis of Early Precambrian Iron Formations – A Review. *Earth-Sci. Rev.* **2021**, 103613. https://doi.org/10.1016/j.earscirev.2021.103613.

(41) Rasmussen, B.; Krapež, B.; Muhling, J. R. Hematite Replacement of Iron-Bearing Precursor Sediments in the 3.46-b.y.-Old Marble Bar Chert, Pilbara Craton, Australia. *Geol. Soc. Am. Bull.* **2014**, *126* (9–10), 1245–1258. https://doi.org/10.1130/B31049.1.

(42) Tosca, N. J.; Jiang, C. Z.; Rasmussen, B.; Muhling, J. Products of the Iron Cycle on the Early Earth. *Free Radic. Biol. Med.* **2019**, *140*, 138–153. https://doi.org/10.1016/j.freeradbiomed.2019.05.005.

(43) Rasmussen, B.; Muhling, J. R. Comment on “Early Archean Biogeochemical Iron Cycling and Nutrient Availability: New Insights from a 3.5 Ga Land-Sea Transition” by Clark M. Johnson, Xin-Yuan Zheng, Tara Djokic, Martin J. Van Kranendonk, Andrew D. Czaja, Eric E. Roden, Brian L. Beard, 2022, Earth-Science Reviews, Https://Doi.Org/10.1016/j.Earscirev.2022.103992. *Earth-Sci. Rev.* **2022**, 104088. https://doi.org/10.1016/j.earscirev.2022.104088.

(44) Muhling, J. R.; Rasmussen, B. Widespread Deposition of Greenalite to Form Banded Iron Formations before the Great Oxidation Event. *Precambrian Res.* **2020**, 105619. https://doi.org/10.1016/j.precamres.2020.105619.

(45) Rasmussen, B.; Muhling, J. R.; Tosca, N. J.; Tsikos, H. Evidence for Anoxic Shallow Oceans at 2.45 Ga: Implications for the Rise of Oxygenic Photosynthesis. *Geology* **2019**. https://doi.org/10.1130/G46162.1.

(46) Rasmussen, B.; Krapež, B.; Muhling, J. R.; Suvorova, A. Precipitation of Iron Silicate Nanoparticles in Early Precambrian Oceans Marks Earth’s First Iron Age. *Geology* **2015**, *43* (4), 303–306. https://doi.org/10.1130/G36309.1.

(47) Rasmussen, B.; Krapež, B.; Meier, D. B. Replacement Origin for Hematite in 2.5 Ga Banded Iron Formation: Evidence for Postdepositional Oxidation of Iron-Bearing Minerals. *Geol. Soc. Am. Bull.* **2014**, B30944.1. https://doi.org/10.1130/B30944.1.

(48) Rasmussen, B.; Muhling, J. R.; Suvorova, A.; Krapež, B. Dust to Dust: Evidence for the Formation of “Primary” Hematite Dust in Banded Iron Formations via Oxidation of Iron Silicate Nanoparticles. *Precambrian Res.* **2016**, *284*, 49–63. https://doi.org/10.1016/j.precamres.2016.07.003.

(49) Frost, C. D.; von Blanckenburg, F.; Schoenberg, R.; Frost, B. R.; Swapp, S. M. Preservation of Fe Isotope Heterogeneities during Diagenesis and Metamorphism of Banded Iron Formation. *Contrib. Mineral. Petrol.* **2006**, *153* (2), 211. https://doi.org/10.1007/s00410-006-0141-0.

(50) Dauphas, N.; John, S. G.; Rouxel, O. Iron Isotope Systematics. *Rev. Mineral. Geochem.* **2017**, *82* (1), 415–510. https://doi.org/10.1515/9783110545630-012.

(51) Heard, A. W.; Dauphas, N. Constraints on the Coevolution of Oxic and Sulfidic Ocean Iron Sinks from Archean–Paleoproterozoic Iron Isotope Records. *Geology* **2020**, *48* (4), 358–362. https://doi.org/10.1130/G46951.1.

(52) Dauphas, N.; Cates, N. L.; Mojzsis, S. J.; Busigny, V. Identification of Chemical Sedimentary Protoliths Using Iron Isotopes in the > 3750 Ma Nuvvuagittuq Supracrustal Belt, Canada. *Earth Planet. Sci. Lett.* **2007**, *254* (3–4), 358–376. https://doi.org/10.1016/j.epsl.2006.11.042.

(53) Dauphas, N.; van Zuilen, M.; Busigny, V.; Lepland, A.; Wadhwa, M.; Janney, P. E. Iron Isotope, Major and Trace Element Characterization of Early Archean Supracrustal Rocks from SW Greenland: Protolith Identification and Metamorphic Overprint. *Geochim. Cosmochim. Acta* **2007**, *71* (19), 4745–4770. https://doi.org/10.1016/j.gca.2007.07.019.

(54) Dauphas, N.; Zuilen, M. van; Wadhwa, M.; Davis, A. M.; Marty, B.; Janney, P. E. Clues from Fe Isotope Variations on the Origin of Early Archean BIFs from Greenland. *Science* **2004**, *306* (5704), 2077–2080. https://doi.org/10.1126/science.1104639.

(55) Beard, B. L.; Handler, R. M.; Scherer, M. M.; Wu, L.; Czaja, A. D.; Heimann, A.; Johnson, C. M. Iron Isotope Fractionation between Aqueous Ferrous Iron and Goethite. *Earth Planet. Sci. Lett.* **2010**, *295* (1), 241–250. https://doi.org/10.1016/j.epsl.2010.04.006.

(56) Bullen, T. D.; White, A. F.; Childs, C. W.; Vivit, D. V.; Schulz, M. S. Demonstration of Significant Abiotic Iron Isotope Fractionation in Nature. *Geology* **2001**, *29* (8), 699–702. https://doi.org/10.1130/0091-7613(2001)029<0699:DOSAII>2.0.CO;2.

(57) Croal, L. R.; Johnson, C. M.; Beard, B. L.; Newman, D. K. Iron Isotope Fractionation by Fe(II)-Oxidizing Photoautotrophic Bacteria 1. *Geochim. Cosmochim. Acta* **2004**, *68* (6), 1227–1242. https://doi.org/10.1016/j.gca.2003.09.011.

(58) Skulan, J. L.; Beard, B. L.; Johnson, C. M. Kinetic and Equilibrium Fe Isotope Fractionation between Aqueous Fe(III) and Hematite. *Geochim. Cosmochim. Acta* **2002**, *66* (17), 2995–3015. https://doi.org/10.1016/S0016-7037(02)00902-X.

(59) Wu, L.; Beard, B. L.; Roden, E. E.; Johnson, C. M. Stable Iron Isotope Fractionation Between Aqueous Fe(II) and Hydrous Ferric Oxide. *Environ. Sci. Technol.* **2011**, *45* (5), 1847–1852. https://doi.org/10.1021/es103171x.

(60) Wiesli, R. A.; Beard, B. L.; Johnson, C. M. Experimental Determination of Fe Isotope Fractionation between Aqueous Fe(II), Siderite and “Green Rust” in Abiotic Systems. *Chem. Geol.* **2004**, *211* (3), 343–362. https://doi.org/10.1016/j.chemgeo.2004.07.002.

(61) Li, W.; Czaja, A. D.; Van Kranendonk, M. J.; Beard, B. L.; Roden, E. E.; Johnson, C. M. An Anoxic, Fe(II)-Rich, U-Poor Ocean 3.46 Billion Years Ago. *Geochim. Cosmochim. Acta* **2013**, *120*, 65–79. https://doi.org/10.1016/j.gca.2013.06.033.

(62) Blanchard, M.; Dauphas, N.; Hu, M. Y.; Roskosz, M.; Alp, E. E.; Golden, D. C.; Sio, C. K.; Tissot, F. L. H.; Zhao, J.; Gao, L.; Morris, R. V.; Fornace, M.; Floris, A.; Lazzeri, M.; Balan, E. Reduced Partition Function Ratios of Iron and Oxygen in Goethite. *Geochim. Cosmochim. Acta* **2015**, *151*, 19–33. https://doi.org/10.1016/j.gca.2014.12.006.

(63) Dauphas, N.; Roskosz, M.; Alp, E. E.; Golden, D. C.; Sio, C. K.; Tissot, F. L. H.; Hu, M. Y.; Zhao, J.; Gao, L.; Morris, R. V. A General Moment NRIXS Approach to the Determination of Equilibrium Fe Isotopic Fractionation Factors: Application to Goethite and Jarosite. *Geochim. Cosmochim. Acta* **2012**, *94*, 254–275. https://doi.org/10.1016/j.gca.2012.06.013.

(64) Nie, N. X.; Dauphas, N.; Alp, E. E.; Zeng, H.; Sio, C. K.; Hu, J. Y.; Chen, X.; Aarons, S. M.; Zhang, Z.; Tian, H.-C.; Wang, D.; Prissel, K. B.; Greer, J.; Bi, W.; Hu, M. Y.; Zhao, J.; Shahar, A.; Roskosz, M.; Teng, F.-Z.; Krawczynski, M. J.; Heck, P. R.; Spear, F. S. Iron, Magnesium, and Titanium Isotopic Fractionations between Garnet, Ilmenite, Fayalite, Biotite, and Tourmaline: Results from NRIXS, Ab Initio, and Study of Mineral Separates from the Moosilauke Metapelite. *Geochim. Cosmochim. Acta* **2021**. https://doi.org/10.1016/j.gca.2021.03.014.

(65) Schauble, E. A.; Rossman, G. R.; Taylor, H. P. Theoretical Estimates of Equilibrium Fe-Isotope Fractionations from Vibrational Spectroscopy. *Geochim. Cosmochim. Acta* **2001**, *65* (15), 2487–2497. https://doi.org/10.1016/S0016-7037(01)00600-7.

(66) Johnson, C. M.; Skulan, J. L.; Beard, B. L.; Sun, H.; Nealson, K. H.; Braterman, P. S. Isotopic Fractionation between Fe(III) and Fe(II) in Aqueous Solutions. *Earth Planet. Sci. Lett.* **2002**, *195* (1–2), 141–153. https://doi.org/10.1016/S0012-821X(01)00581-7.

(67) Welch, S. A.; Beard, B. L.; Johnson, C. M.; Braterman, P. S. Kinetic and Equilibrium Fe Isotope Fractionation between Aqueous Fe(II) and Fe(III). *Geochim. Cosmochim. Acta* **2003**, *67* (22), 4231–4250. https://doi.org/10.1016/S0016-7037(03)00266-7.

(68) Anbar, A. D.; Jarzecki, A. A.; Spiro, T. G. Theoretical Investigation of Iron Isotope Fractionation between Fe(H2O)63+ and Fe(H2O)62+: Implications for Iron Stable Isotope Geochemistry. *Geochim. Cosmochim. Acta* **2005**, *69* (4), 825–837. https://doi.org/10.1016/j.gca.2004.06.012.

(69) Domagal-Goldman, S. D.; Kubicki, J. D. Density Functional Theory Predictions of Equilibrium Isotope Fractionation of Iron Due to Redox Changes and Organic Complexation. *Geochim. Cosmochim. Acta* **2008**, *72* (21), 5201–5216. https://doi.org/10.1016/j.gca.2008.05.066.

(70) Hill, P. S.; Schauble, E. A. Modeling the Effects of Bond Environment on Equilibrium Iron Isotope Fractionation in Ferric Aquo-Chloro Complexes. *Geochim. Cosmochim. Acta* **2008**, *72* (8), 1939–1958. https://doi.org/10.1016/j.gca.2007.12.023.

(71) Ottonello, G.; Zuccolini, M. V. Ab-Initio Structure, Energy and Stable Fe Isotope Equilibrium Fractionation of Some Geochemically Relevant H–O–Fe Complexes. *Geochim. Cosmochim. Acta* **2009**, *73* (21), 6447–6469. https://doi.org/10.1016/j.gca.2009.06.034.

(72) Rustad, J. R.; Dixon, D. A. Prediction of Iron-Isotope Fractionation Between Hematite (α-Fe2O3) and Ferric and Ferrous Iron in Aqueous Solution from Density Functional Theory. *J. Phys. Chem. A* **2009**, *113* (44), 12249–12255. https://doi.org/10.1021/jp9065373.

(73) Blanchard, M.; Poitrasson, F.; Méheut, M.; Lazzeri, M.; Mauri, F.; Balan, E. Iron Isotope Fractionation between Pyrite (FeS2), Hematite (Fe2O3) and Siderite (FeCO3): A First-Principles Density Functional Theory Study. *Geochim. Cosmochim. Acta* **2009**, *73* (21), 6565–6578. https://doi.org/10.1016/j.gca.2009.07.034.

(74) Crosby; Roden Eric E.; Johnson Clark M.; Beard Brian L. The Mechanisms of Iron Isotope Fractionation Produced during Dissimilatory Fe(III) Reduction by Shewanella Putrefaciens and Geobacter Sulfurreducens. *Geobiology* **2007**, *5* (2), 169–189. https://doi.org/10.1111/j.1472-4669.2007.00103.x.

(75) Swanner, E. D.; Bayer, T.; Wu, W.; Hao, L.; Obst, M.; Sundman, A.; Byrne, J. M.; Michel, F. M.; Kleinhanns, I. C.; Kappler, A.; Schoenberg, R. Iron Isotope Fractionation during Fe(II) Oxidation Mediated by the Oxygen-Producing Marine Cyanobacterium Synechococcus PCC 7002. *Environ. Sci. Technol.* **2017**. https://doi.org/10.1021/acs.est.6b05833.

(76) Guggenheim, S.; Bailey, S. W.; Eggleton, R. A.; Wilkes, P. STRUCTURAL ASPECTS OF GREENALITE AND RELATED MINERALS. *Can. Mineral.* **1982**, *20*, 1–18.

(77) Schwertmann, U.; Cornell, R. M. Ferrihydrite. In *Iron Oxides in the Laboratory*; John Wiley & Sons, Ltd, 2000; pp 103–112. https://doi.org/10.1002/9783527613229.ch08.

(78) Hammersley, A. P. FIT2D: A Multi-Purpose Data Reduction, Analysis and Visualization Program. *J. Appl. Crystallogr.* **2016**, *49* (2), 646–652. https://doi.org/10.1107/S1600576716000455.

(79) Janney, D. E.; Cowley, J. M.; Buseck, P. R. Transmission Electron Microscopy of Synthetic 2- and 6-Line Ferrihydrite. *Clays Clay Miner.* **2000**, *48* (1), 111–119. https://doi.org/10.1346/CCMN.2000.0480114.

(80) Seto, M.; Yoda, Y.; Kikuta, S.; Zhang, X. W.; Ando, M. Observation of Nuclear Resonant Scattering Accompanied by Phonon Excitation Using Synchrotron Radiation. *Phys. Rev. Lett.* **1995**, *74* (19), 3828–3831. https://doi.org/10.1103/PhysRevLett.74.3828.

(81) Sturhahn, W.; Toellner, T. S.; Alp, E. E.; Zhang, X.; Ando, M.; Yoda, Y.; Kikuta, S.; Seto, M.; Kimball, C. W.; Dabrowski, B. Phonon Density of States Measured by Inelastic Nuclear Resonant Scattering. *Phys. Rev. Lett.* **1995**, *74* (19), 3832–3835. https://doi.org/10.1103/PhysRevLett.74.3832.

(82) Hu, M. Y.; Toellner, T. S.; Dauphas, N.; Alp, E. E.; Zhao, J. Moments in Nuclear Resonant Inelastic X-Ray Scattering and Their Applications. *Phys. Rev. B* **2013**, *87* (6), 064301. https://doi.org/10.1103/PhysRevB.87.064301.

(83) Polyakov, V. B.; Mineev, S. D. The Use of Mössbauer Spectroscopy in Stable Isotope Geochemistry. *Geochim. Cosmochim. Acta* **2000**, *64* (5), 849–865. https://doi.org/10.1016/S0016-7037(99)00329-4.

(84) Dauphas, N.; Hu, M. Y.; Baker, E. M.; Hu, J.; Tissot, F. L. H.; Alp, E. E.; Roskosz, M.; Zhao, J.; Bi, W.; Liu, J.; Lin, J.-F.; Nie, N. X.; Heard, A. SciPhon: A Data Analysis Software for Nuclear Resonant Inelastic X-Ray Scattering with Applications to Fe, Kr, Sn, Eu and Dy. *J. Synchrotron Radiat.* **2018**, *25* (5), 1581–1599. https://doi.org/10.1107/S1600577518009487.

(85) Sturhahn, W. CONUSS and PHOENIX: Evaluation of Nuclear Resonant Scattering Data. *Hyperfine Interact.* **2000**, *125* (1), 149–172. https://doi.org/10.1023/A:1012681503686.

(86) van Bürck, U.; Siddons, D. P.; Hastings, J. B.; Bergmann, U.; Hollatz, R. Nuclear Forward Scattering of Synchrotron Radiation. *Phys. Rev. B* **1992**, *46* (10), 6207–6211. https://doi.org/10.1103/PhysRevB.46.6207.

(87) Alp, E. E.; Sturhahn, W.; Toellner, T. S. Synchrotron Mossbauer Spectroscopy of Powder Samples. *Nucl. Instrum. Methods Phys. Res. Sect. B Beam Interact. Mater. At.* **1995**, *97* (1–4), 526–529. https://doi.org/10.1016/0168-583X(94)00743-8.

(88) Evans, B. W.; Dyar, M. D.; Kuehner, S. M. Implications of Ferrous and Ferric Iron in Antigorite. *Am. Mineral.* **2012**, *97* (1), 184–196. https://doi.org/10.2138/am.2012.3926.

(89) Tutolo, B. M.; Seyfried, W. E.; Tosca, N. J. A Seawater Throttle on H2 Production in Precambrian Serpentinizing Systems. *Proc. Natl. Acad. Sci.* **2020**. https://doi.org/10.1073/pnas.1921042117.

(90) Tutolo, B. M.; Evans, B. W.; Kuehner, S. M. Serpentine–Hisingerite Solid Solution in Altered Ferroan Peridotite and Olivine Gabbro. *Minerals* **2019**, *9* (1), 47. https://doi.org/10.3390/min9010047.

(91) Michel, F. M.; Ehm, L.; Antao, S. M.; Lee, P. L.; Chupas, P. J.; Liu, G.; Strongin, D. R.; Schoonen, M. A. A.; Phillips, B. L.; Parise, J. B. The Structure of Ferrihydrite, a Nanocrystalline Material. *Science* **2007**, *316* (5832), 1726–1729. https://doi.org/10.1126/science.1142525.

(92) Drits, V. A.; Sakharov, B. A.; Salyn, A. L.; Manceau, A. Structural Model for Ferrihydrite. *Clay Miner.* **1993**, *28* (2), 185–207. https://doi.org/10.1180/claymin.1993.028.2.02.

(93) Sassi, M.; Chaka, A. M.; Rosso, K. M. Ab Initio Thermodynamics Reveals the Nanocomposite Structure of Ferrihydrite. *Commun. Chem.* **2021**, *4* (1), 1–10. https://doi.org/10.1038/s42004-021-00562-7.

(94) Giannozzi, P.; Baroni, S.; Bonini, N.; Calandra, M.; Car, R.; Cavazzoni, C.; Ceresoli, D.; Chiarotti, G. L.; Cococcioni, M.; Dabo, I.; Dal Corso, A.; de Gironcoli, S.; Fabris, S.; Fratesi, G.; Gebauer, R.; Gerstmann, U.; Gougoussis, C.; Kokalj, A.; Lazzeri, M.; Martin-Samos, L.; Marzari, N.; Mauri, F.; Mazzarello, R.; Paolini, S.; Pasquarello, A.; Paulatto, L.; Sbraccia, C.; Scandolo, S.; Sclauzero, G.; Seitsonen, A. P.; Smogunov, A.; Umari, P.; Wentzcovitch, R. M. QUANTUM ESPRESSO: A Modular and Open-Source Software Project for Quantum Simulations of Materials. *J. Phys. Condens. Matter Inst. Phys. J.* **2009**, *21* (39), 395502. https://doi.org/10.1088/0953-8984/21/39/395502.

(95) Perdew, J. P.; Burke, K.; Ernzerhof, M. Generalized Gradient Approximation Made Simple. *Phys. Rev. Lett.* **1996**, *77* (18), 3865–3868. https://doi.org/10.1103/PhysRevLett.77.3865.

(96) Garrity, K. F.; Bennett, J. W.; Rabe, K. M.; Vanderbilt, D. Pseudopotentials for High-Throughput DFT Calculations. *Comput. Mater. Sci.* **2014**, *81*, 446–452. https://doi.org/10.1016/j.commatsci.2013.08.053.

(97) Monkhorst, H. J.; Pack, J. D. Special Points for Brillouin-Zone Integrations. *Phys. Rev. B* **1976**, *13* (12), 5188–5192. https://doi.org/10.1103/PhysRevB.13.5188.

(98) Pinney, N.; Kubicki, J. D.; Middlemiss, D. S.; Grey, C. P.; Morgan, D. Density Functional Theory Study of Ferrihydrite and Related Fe-Oxyhydroxides. *Chem. Mater.* **2009**, *21* (24), 5727–5742. https://doi.org/10.1021/cm9023875.

(99) Coey, J. M. D.; Ballet, O.; Moukarika, A.; Soubeyroux, J. L. Magnetic Properties of Sheet Silicates; 1:1 Layer Minerals. *Phys. Chem. Miner.* **1981**, *7* (3), 141–148. https://doi.org/10.1007/BF00308232.

(100) Cococcioni, M.; de Gironcoli, S. Linear Response Approach to the Calculation of the Effective Interaction Parameters in the $\mathrm{LDA}+\mathrm{U}$ Method. *Phys. Rev. B* **2005**, *71* (3), 035105. https://doi.org/10.1103/PhysRevB.71.035105.

(101) Kulik, H. J.; Cococcioni, M.; Scherlis, D. A.; Marzari, N. Density Functional Theory in Transition-Metal Chemistry: A Self-Consistent Hubbard U Approach. *Phys. Rev. Lett.* **2006**, *97* (10), 103001. https://doi.org/10.1103/PhysRevLett.97.103001.

(102) Blanchard, M.; Balan, E.; Schauble, E. A. Equilibrium Fractionation of Non-Traditional Isotopes: A Molecular Modeling Perspective. *Rev. Mineral. Geochem.* **2017**, *82* (1), 27–63. https://doi.org/10.2138/rmg.2017.82.2.

(103) Baroni, S.; de Gironcoli, S.; Dal Corso, A.; Giannozzi, P. Phonons and Related Crystal Properties from Density-Functional Perturbation Theory. *Rev. Mod. Phys.* **2001**, *73* (2), 515–562. https://doi.org/10.1103/RevModPhys.73.515.

(104) Aarons, S. M.; Dauphas, N.; Blanchard, M.; Zeng, H.; Nie, N. X.; Johnson, A. C.; Greber, N. D.; Hopp, T. Clues from Ab Initio Calculations on Titanium Isotopic Fractionation in Tholeiitic and Calc-Alkaline Magma Series. *ACS Earth Space Chem.* **2021**, *5* (9), 2466–2480. https://doi.org/10.1021/acsearthspacechem.1c00172.

(105) Dauphas, N.; Nie, N. X.; Blanchard, M.; Zhang, Z. J.; Zeng, H.; Hu, J. Y.; Meheut, M.; Visscher, C.; Canup, R.; Hopp, T. The Extent, Nature, and Origin of K and Rb Depletions and Isotopic Fractionations in Earth, the Moon, and Other Planetary Bodies. *Planet. Sci. J.* **2022**, *3* (2), 29. https://doi.org/10.3847/PSJ/ac2e09.

(106) Gruner, J. W. The Structure and Chemical Composition of Greenalite. *Am. Mineral.* **1936**, *21* (7), 449–455.

(107) Lee, S.; Xu, H. One-Step Route Synthesis of Siliceous Six-Line Ferrihydrite: Implication for the Formation of Natural Ferrihydrite. *ACS Earth Space Chem.* **2019**, *3* (4), 503–509. https://doi.org/10.1021/acsearthspacechem.8b00179.

(108) Beard, B. L.; Johnson, C. M.; Damm, K. L. V.; Poulson, R. L. Iron Isotope Constraints on Fe Cycling and Mass Balance in Oxygenated Earth Oceans. *Geology* **2003**, *31* (7), 629–632. https://doi.org/10.1130/0091-7613(2003)031<0629:IICOFC>2.0.CO;2.

(109) Severmann, S.; Johnson, C. M.; Beard, B. L.; German, C. R.; Edmonds, H. N.; Chiba, H.; Green, D. R. H. The Effect of Plume Processes on the Fe Isotope Composition of Hydrothermally Derived Fe in the Deep Ocean as Inferred from the Rainbow Vent Site, Mid-Atlantic Ridge, 36°14′N. *Earth Planet. Sci. Lett.* **2004**, *225* (1), 63–76. https://doi.org/10.1016/j.epsl.2004.06.001.

(110) Johnson, C. M.; Zheng, X.-Y.; Djokic, T.; Van Kranendonk, M. J.; Czaja, A. D.; Roden, E. E.; Beard, B. L. Early Archean Biogeochemical Iron Cycling and Nutrient Availability: New Insights from a 3.5 Ga Land-Sea Transition. *Earth-Sci. Rev.* **2022**, *228*, 103992. https://doi.org/10.1016/j.earscirev.2022.103992.

(111) Heard, A. W.; Bekker, A.; Kovalick, A.; Tsikos, H.; Ireland, T.; Dauphas, N. Oxygen Production and Rapid Iron Oxidation in Stromatolites Immediately Predating the Great Oxidation Event. *Earth Planet. Sci. Lett.* **2022**, *582*, 117416. https://doi.org/10.1016/j.epsl.2022.117416.

(112) Hiebert, R. S.; Bekker, A.; Houlé, M. G.; Rouxel, O. J. Depositional Setting of the Late Archean Fe Oxide- and Sulfide-Bearing Chert and Graphitic Argillite in the Shaw Dome, Abitibi Greenstone Belt, Canada. *Precambrian Res.* **2018**, *311*, 98–116. https://doi.org/10.1016/j.precamres.2018.04.004.

(113) Nie, N. X.; Dauphas, N.; Villalon, K. L.; Liu, N.; Heard, A. W.; Morris, R. V.; Mertzman, S. A. Iron Isotopic and Chemical Tracing of Basalt Alteration and Hematite Spherule Formation in Hawaii: A

Prospective Study for Mars. *Earth Planet. Sci. Lett.* **2020**, *544*, 116385. https://doi.org/10.1016/j.epsl.2020.116385.

(114) Planavsky, N. J.; Asael, D.; Hofmann, A.; Reinhard, C. T.; Lalonde, S. V.; Knudsen, A.; Wang, X.; Ossa Ossa, F.; Pecoits, E.; Smith, A. J. B.; Beukes, N. J.; Bekker, A.; Johnson, T. M.; Konhauser, K. O.; Lyons, T. W.; Rouxel, O. J. Evidence for Oxygenic Photosynthesis Half a Billion Years before the Great Oxidation Event. *Nat. Geosci.* **2014**, *7* (4), 283–286. https://doi.org/10.1038/ngeo2122.

(115) Thibon, F.; Blichert-Toft, J.; Tsikos, H.; Foden, J.; Albalat, E.; Albarede, F. Dynamics of Oceanic Iron Prior to the Great Oxygenation Event. *Earth Planet. Sci. Lett.* **2019**, *506*, 360–370. https://doi.org/10.1016/j.epsl.2018.11.016.

(116) Ingalls, M.; Grotzinger, J. P.; Present, T.; Rasmussen, B.; Fischer, W. W. Carbonate-Associated Phosphate (CAP) Indicates Elevated Phosphate Availability in Neoarchean Shallow Marine Environments. *Geophys. Res. Lett.* **2022**, *49* (6), e2022GL098100. https://doi.org/10.1029/2022GL098100.

(117) Rasmussen, B.; Muhling, J. R.; Suvorova, A.; Fischer, W. W. Apatite Nanoparticles in 3.46–2.46 Ga Iron Formations: Evidence for Phosphorus-Rich Hydrothermal Plumes on Early Earth. *Geology* **2021**, *49* (6), 647–651. https://doi.org/10.1130/G48374.1.

(118) Reinhard, C. T.; Planavsky, N. J.; Gill, B. C.; Ozaki, K.; Robbins, L. J.; Lyons, T. W.; Fischer, W. W.; Wang, C.; Cole, D. B.; Konhauser, K. O. Evolution of the Global Phosphorus Cycle. *Nature* **2017**, *541* (7637), 386–389. https://doi.org/10.1038/nature20772.

FOR TOC ONLY

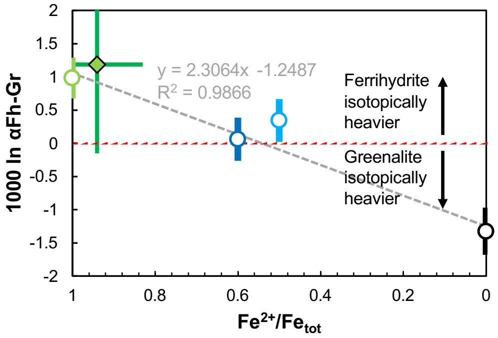

2
1.5
1
0.5
0
-0.5
-1
-1.5
-2
1000 ln αFh-Gr
y = 2.3064x -1.2487
$R^2 = 0.9866$
Ferrihydrite isotopically heavier
Greenalite isotopically heavier
1
0.8
0.6
0.4
0.2
0
Fe^{2+}/Fe_{tot}